A Runge-Kutta-Chebyshev SPH algorithm for elastodynamics

Lisha He* **Mohammed Seaid†**

Abstract

A stable and accurate Smoothed Particle Hydrodynamics (SPH) method is proposed for solving elastodynamics in solid mechanics. The SPH method is mesh-free and it promises to overcome most of disadvantages of the traditional finite element techniques. The absence of a mesh makes the SPH method very attractive for those problems involving large deformations, moving boundaries and crack propagation. However, the conventional SPH method still has significant limitations that prevent its acceptance among researchers and engineers, namely the stability and computational costs. In approximating unsteady problems using the SPH method, attention should be given to the choice of time integration schemes as accuracy and efficiency of the SPH solution may be limited by the timesteps used in the simulation. This study presents an attempt to reconstruct unconditionally stable SPH method for elastodynamics. To achieve this objective we implement an explicit Runge-Kutta Chebyshev scheme with extended stages in the SPH method. This time stepping scheme adds in a natural way a stabilizing stage to the conventional Runge-Kutta method using the Chebyshev polynomials. Numerical results are shown for several test problems in elastodynamics. For the considered elastic regimes, the obtained results demonstrate the ability of our new algorithm to better maintain the shape of the solution in the presence of shocks.

Keywords. SPH Method; Runge-Kutta-Chebyshev; Elastodynamics; Numerical simulation

1 Introduction

Developing efficient numerical methods for solving solids and structures under large deformation has attracted many researchers in the field of elastodynamics. The emphasis in most of these techniques is on accurate simulations of deformation for complex engineering applications, see for example [5, 35, 2, 17, 40]. Numerical treatment of the elastodynamic equations often present difficulties due to the presence of advective terms and the coupling between the stress and displacement. In many elastodynamic problems, the advective term is a source of computational difficulties and nonphysical oscillations. It is known that standard Eulerian methods do not handle advective terms very well unless small timesteps and highly refined grids are used in simulations. Most of these methods uses explicit time stepping, incorporate some upstream weighting in their formulations to stabilize the numerical procedure and are relatively easy to formulate and to implement.

Mesh-based techniques such as finite element and finite volume methods have been widely used for solving partial differential equations governing solid mechanics. However, the accuracy of these methods is affected by the quality of meshes, which hinders their applications to solving real problems in complex domains and with moving boundaries. Recently, some significant developments in meshless methods for solving linear and nonlinear partial differential equations have been achieved.

*School of Engineering and Computing Sciences, University of Durham, South Road, Durham DH1 3LE, UK *E-mail:* lisha.he@durham.ac.uk

†School of Engineering and Computing Sciences, University of Durham, South Road, Durham DH1 3LE, UK *E-mail:* m.seaid@durham.ac.uk

For instance, the meshless local Petrov-Galerkin and local boundary integral equations methods were studied in [4, 33, 23]. These two methods basically transformed the original problem into a local weak formulation and the shape functions were constructed from using the moving least-squares approximation to interpolate the solution variables. The Smoothed Particle Hydrodynamics (SPH) method was first developed in [22, 12]. In this method, the continuum domain is discretized into particles carrying the field variables. These variables are calculated from the contribution of the neighboring particles by means of a kernel function. The SPH is a truly meshless method based on the transformation of differential equations into integral ones which are then discretized using a distribution of moving particles. The SPH method has been traditionally applied in computational fluid dynamics. In recent years, there has been a growing interest in applying SPH method to a wide variety of problems in solid mechanics [21]. The main feature of SPH method is that it is a particle based technique and does not require any underlying grid structure to represent the problem geometry. This avoids the difficulties associated with traditional mesh-based methods such as maintaining the integrity and quality of the mesh under large deformation. The mesh-free nature of the SPH method makes it ideally suited to modeling processes that involve large deformations and discontinuities such as fracture, fragmentation and metal forming among others. It has given relatively good results in many applications in both fluid and solid dynamics. Application of the SPH methods to steady and time-dependent models has also been investigated, see for example [13, 1, 41, 39, 6].

When approximating unsteady solid mechanics using the SPH method, attention should be given to the selection of the time integration scheme. A fully implicit integration of the governing equations often leads to methods that are unconditionally stable however, this procedure involves the simultaneous solution of a large number of coupled linear equations. Moreover, for accuracy reasons the timestep cannot be taken arbitrarily large, so these methods often become impractical. On the other hand, the limitation of standard explicit numerical methods for elastodynamic equations is the stability restriction imposed on the timestep by the Courant-Friedrichs-Lewy (CFL) conditions. For instance the explicit first-order Euler, second-order predictor-corrector, and the fourth-order Runge-Kutta methods have been widely used in SPH simulations, see for example [16, 13, 9]. However, time truncation errors dominate the accuracy of the solutions obtained by these methods and are subjected to the CFL condition, which put a severe restriction on the size of timesteps taken in the numerical simulations. The Runge-Kutta Chebyshev (RKC) method was first proposed in [7] and is suitable for time integration of semi-discretized unsteady partial differential equations, compare [37]. The RKC method adds in a natural way a stabilizing stage to the explicit conventional Runge-Kutta method using the Chebyshev polynomials. It is not subjected to CFL restrictions and generates accurate solutions without oscillations and excessive numerical diffusion even if large timesteps are taken in simulations. The emphasis in this work is on the time integration of the resultant system of ordinary differential equations (ODE) generated from the SPH space discretization of the transient elastodynamic problems. To the best of our knowledge, solving elastodynamics using combined SPH and RKC method is reported for the first time.

The remainder of the paper is organized as follows. In Section 2 we formulate the SPH method for elastodynamics. This section covers all relevant ingredients for the SPH method applied to elastodynamics. Then, we introduce the RKC scheme and its implementation for solving the SPH equations for elsatodynamic problems in Section 3. Section 4 presents the results and application of our SPH algorithm. In particular, we consider an elastodynamic problem with known analytical solution to quantify the accuracy of the new SPH method and an elastic beam under oscillatory deformation. The proposed SPH method is also applied to simulate an elastic plate with a void under compression. The presented results clearly show the overall performance of the proposed Runge-Kutta Chebyshev SPH method. Finally, we conclude with some remarks in Section 5.

2 SPH method for elastodynamics

The principal idea of the SPH method, is to approximate a generic variable f at the point $\mathbf{X}_i$ in the computational domain using the contributions of the neighboring particles within a support domain V as

$$f_i = \sum_{j=1}^{N} f_j W_{ji} \Delta \mathrm{V}_j = \sum_{j=1}^{N} \frac{m_j}{\rho_j} f_j W_{ij}, \tag{1}$$

where the subscript j indicates a neighboring particle to the considered particle i, N is the total number of particles in the domain V, W_{ij} is the smoothing (kernel) function, $\Delta \mathrm{V} = m/\rho$ represents the volume of each particle inside the support domain V, m and ρ are the mass and density, respectively. In general, the smoothing function should be compact, normalized and satisfies delta conditions [21, 20]. An illustration of the smoothing function is shown in Figure 1 where κh represents the radius of the support domain with κ is a constant and h is the smoothing length. In the present work, we use the B-spline function frequently applied as a smoothing function in SPH simulations, see for example [26]. The B-spline function is defined as

$$W(\mathbf{r}_{ij}, h) = \alpha_d \begin{cases} \frac{2}{3} - \widetilde{r}^2 + \frac{1}{2}\widetilde{r}^3, & \text{if} \quad \widetilde{r} < 1, \\ 6(2 - \widetilde{r})^3, & \text{if} \quad 1 \leq \widetilde{r} < 2, \\ 0, & \text{if} \quad \widetilde{r} > 2, \end{cases} \tag{2}$$

where $\alpha_d = \dfrac{1}{h}$, $\dfrac{15}{7\pi h^2}$ and $\dfrac{3}{2\pi h^3}$ for one-, two-, and three-dimensional problems, respectively. Here $\mathbf{r}_{ij} = |\mathbf{X}_i - \mathbf{X}_j|$, with $\mathbf{X}_i$ and $\mathbf{X}_j$ represent respectively, the coordinates of particle i and j, and $\widetilde{r}$ denotes the relative distance between particles i and j *i.e.*,

$$\widetilde{r} = \frac{|\mathbf{X}_i - \mathbf{X}_j|}{h}.$$

Note that the radius of the support domain in this smoothing function is $2h$ and when $|\mathbf{r}_{ij}| \geq 2h$ the smoothing function vanishes which means that there is no influence between particles i and j. It is therefore evident that the smoothing length h significantly influences the accuracy and efficiency of SPH simulations. In the current study, the smoothing length is set to $h = 1.5\Delta d$, with Δd is the initial spacing between particles.

The spatial derivatives of a generic variable f can be approximated by applying the derivative operator to the approximation (1) and using the Gauss theorem to obtain

$$\nabla f_i = \sum_{j=1}^{N} \frac{m_j}{\rho_j} f_j \nabla W_{ij}. \tag{3}$$

Obviously, for a particle near the boundary, the support domain lacks sufficient neighboring particles, compare Figure 2 for an illustration. To overcome this drawback we correct the approximation (1) using the kernel gradient correction proposed in [34]. This correction procedure is based on the normalized from

$$\sum_{j=1}^{N} \frac{m_j}{\rho_j} (\mathbf{X}_j - \mathbf{X}_i) \otimes \nabla W_{ij} = \mathbf{I},$$

where $\mathbf{I}$ is the diagonal unit matrix. The kernel gradient correction is calculated by multiplying the original gradient of smoothing function by an invertible matrix $\mathbf{L}_i$ to restore first-order completeness as

$$\widetilde{\nabla} W_{ij} = \mathbf{L}_i^{-1} \nabla W_{ij},$$

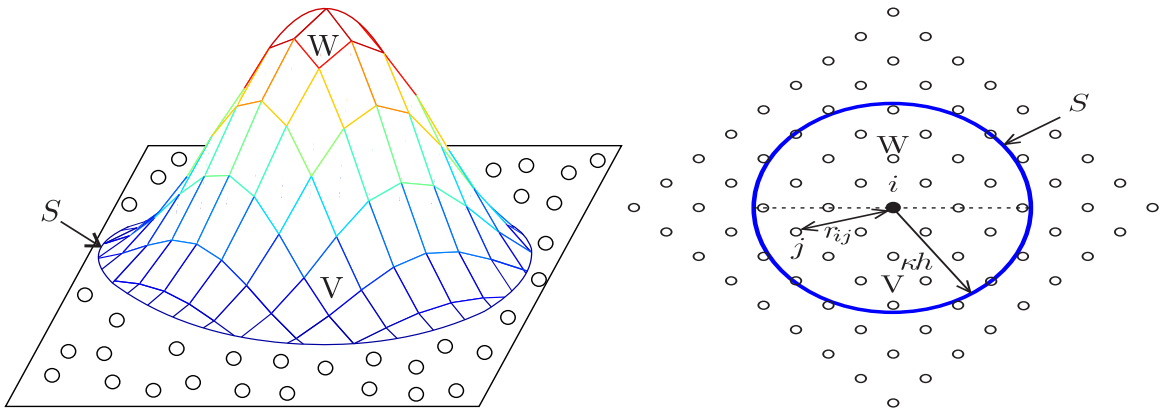

Figure 1: Illustration of the support domain V and the smoothing function W used in the SPH approximation.

where

$$\mathbf{L}_i = \sum_{j=1}^{N} \frac{m_j}{\rho_j} \nabla W_{ij} \otimes (\mathbf{X}_j - \mathbf{X}_i)\,.$$

For two-dimensional problems, the reversible matrix is obtained by

$$\mathbf{L}_i = \begin{pmatrix} \displaystyle\sum_{j=1}^{N} \frac{m_j}{\rho_j} x_{ji} \frac{\partial W_{ij}}{\partial x_i} & \displaystyle\sum_{j=1}^{N} \frac{m_j}{\rho_j} y_{ji} \frac{\partial W_{ij}}{\partial x_i} \\ \displaystyle\sum_{j=1}^{N} \frac{m_j}{\rho_j} x_{ji} \frac{\partial W_{ij}}{\partial y_i} & \displaystyle\sum_{j=1}^{N} \frac{m_j}{\rho_j} y_{ji} \frac{\partial W_{ij}}{\partial y_i} \end{pmatrix}.$$

Therefore, the approximation of the derivative of a function is given by

$$\nabla f_i = \sum_{j=1}^{N} \frac{m_j}{\rho_j} f_j \widetilde{\nabla} W_{ij}. \tag{4}$$

Notice that the second derivative of the kernel function (2) is continuous and the leading truncation error term is of order $\mathcal{O}(h^2)$. The finite aspect of the kernel support means that only a limited number of neighboring particles plays a role in all the sums in the conservation equations. In the current study, this step is achieved by using the kd-tree searching method, see [15] among others.

2.1 Application to elastodynamic equations

In this section we formulate the SPH method for the partial differential equations governing elastodynamics in solid mechanics. These equations consist of the conservation of mass and momentum as

$$\begin{aligned} \frac{D\rho}{Dt} &= -\rho \nabla \cdot \mathbf{v}, \\ \frac{D\mathbf{v}}{Dt} &= \frac{1}{\rho} \nabla \boldsymbol{\sigma} + \mathbf{g}, \end{aligned} \tag{5}$$

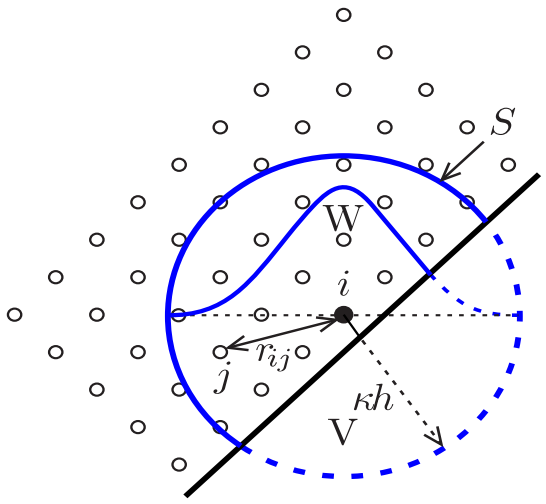

Figure 2: Truncation of the support domain and the kernel function on the boundary.

where $\nabla = \left(\frac{\partial}{\partial x}, \frac{\partial}{\partial y}\right)^T$ is the gradient operator, $\mathbf{g}$ is the acceleration due to body forces such as gravity, ρ is the density, $\mathbf{v} = (v_x, v_y)^T$ is the velocity, $\boldsymbol{\sigma}$ is the stress tensor and $\frac{D}{Dt} = \frac{\partial}{\partial t} + \nabla \cdot \mathbf{v}$ is the total derivative. Using the product rule of differentiation and the definition

$$\nabla \cdot \boldsymbol{\sigma} = \frac{\partial \sigma^{xx}}{\partial x} + \frac{\partial \sigma^{xy}}{\partial y}\frac{\partial \sigma^{xy}}{\partial x} + \frac{\partial \sigma^{yy}}{\partial y},$$

the term $\frac{1}{\rho}\nabla \cdot \boldsymbol{\sigma}$ in (5) can be replaced by

$$\frac{1}{\rho}\nabla \cdot \boldsymbol{\sigma} = \nabla \cdot \left(\frac{\boldsymbol{\sigma}}{\rho}\right) + \frac{\boldsymbol{\sigma}}{\rho^2}\nabla\left(\frac{1}{\rho}\right).$$

For elastodynamic problems considered in this work, the total strain rate is given by

$$\dot{\boldsymbol{\varepsilon}} = \frac{1}{2}\left(\nabla \mathbf{v} + (\nabla \mathbf{v})^T\right), \tag{6}$$

and according to the Hooke's law, we can write stress tensor as

$$\dot{\boldsymbol{\sigma}} = 2G\dot{\boldsymbol{e}} + K\Big(tr\left(\dot{\boldsymbol{\varepsilon}}\right)\Big)\mathbf{I}, \tag{7}$$

where $\dot{\boldsymbol{e}} = \dot{\boldsymbol{\varepsilon}} - \frac{1}{3}tr(\dot{\boldsymbol{\varepsilon}})\mathbf{I}$ is the deviatoric strain rate tensor and $tr(\dot{\boldsymbol{\varepsilon}}) = \dot{\varepsilon}^{xx} + \dot{\varepsilon}^{yy}$; I is the kronecker's delta tensor, K is the elastic bulk modulus and G is the shear modulus which can be represented by the Young's modulus E and the Poisson's ratio ν as

$$K = \frac{E}{3(1-2\nu)} \qquad \text{and} \quad G = \frac{E}{2(1+\nu)}.$$

It should be stressed that when handling a large deformation problem, the Jaumann stress rate $\hat{\dot{\boldsymbol{\sigma}}}$, introduced in [14] to account for the influence of rotation on the constitutive relations, is adopted in our simulations to introduce the influence of rotation on the constitutive relations as

$$\hat{\dot{\boldsymbol{\sigma}}} = \dot{\boldsymbol{\sigma}} + \boldsymbol{\sigma}\boldsymbol{\omega} - \boldsymbol{\omega}\boldsymbol{\sigma}, \tag{8}$$

Then, equation (7) becomes

$$\dot{\boldsymbol{\sigma}} = 2G\dot{\mathbf{e}} + K\Big(tr(\dot{\boldsymbol{\varepsilon}})\Big)\mathbf{I} - \boldsymbol{\sigma}\boldsymbol{\omega} + \boldsymbol{\omega}\boldsymbol{\sigma}, \tag{9}$$

where $\boldsymbol{\omega}$ is the rotation tensor and it can be represented by the velocity gradient as

$$\boldsymbol{\omega} = \frac{1}{2}\left(\nabla\mathbf{v} - (\nabla\mathbf{v})^T\right). \tag{10}$$

The system (5) is to be solved in a bounded spatial domain and for a time interval $(0, T]$ endowed with given initial and boundary conditions. In practice, these conditions are problem dependent and their discussion is postponed to section 4 where numerical examples are discussed.

To discretize the equations (5) in space we first cover the computational domain with a set of particles and the velocity gradient is approximated as

$$\nabla\mathbf{v}_i = \sum_{j=1}^{N} \frac{m_j}{\rho_j}\mathbf{v}_j\widetilde{\nabla}W_{ij}. \tag{11}$$

Since $\displaystyle\sum_{j=1}^{N} \frac{m_j}{\rho_j}\widetilde{\nabla}W_{ij} = 0$,

$$\sum_{j=1}^{N} \frac{m_j}{\rho_j}(\mathbf{v}_j - \mathbf{v}_i)\widetilde{\nabla}W_{ij} = \sum_{j=1}^{N} \frac{m_j}{\rho_j}\mathbf{v}_j\widetilde{\nabla}W_{ij} - \mathbf{v}_i\sum_{j=1}^{N} \frac{m_j}{\rho_j}\widetilde{\nabla}W_{ij} = \sum_{j=1}^{N} \frac{m_j}{\rho_j}\mathbf{v}_j\widetilde{\nabla}W_{ij},$$

the approximation (11) reduces to

$$\nabla\mathbf{v}_i = \sum_{j=1}^{N} \frac{m_j}{\rho_j}(\mathbf{v}_j - \mathbf{v}_i)\widetilde{\nabla}W_{ij}. \tag{12}$$

Hence, the spatial discretization of the equations (5) using the SPH method results in

$$\begin{aligned} \frac{D\rho_i}{Dt} &= -\rho_i\sum_{j=1}^{N} \frac{m_j}{\rho_j}(\mathbf{v}_j - \mathbf{v}_i)\cdot\widetilde{\nabla}W_{ij}, \\ \frac{D\mathbf{v}_i}{Dt} &= \sum_{j=1}^{N} m_j\left(\frac{\boldsymbol{\sigma}_j}{\rho_j^2} + \frac{\boldsymbol{\sigma}_i}{\rho_i^2}\right)\widetilde{\nabla}W_{ij}. \end{aligned} \tag{13}$$

The stress rate of small and large deformations (7) and (9) can also be expressed by the SPH approximation of the velocity field as

$$\frac{D\boldsymbol{\sigma}_i}{Dt} = 2G\dot{\mathbf{e}}_i + K\Big(tr(\dot{\boldsymbol{\varepsilon}}_i)\Big)\mathbf{I}, \tag{14}$$

and

$$\frac{D\boldsymbol{\sigma}_i}{Dt} = 2G\dot{\mathbf{e}}_i + K\Big(tr(\dot{\boldsymbol{\varepsilon}}_i)\Big)\mathbf{I} - \boldsymbol{\sigma}_i\boldsymbol{\omega}_i + \boldsymbol{\omega}_i\boldsymbol{\sigma}_i, \tag{15}$$

respectively. Here $\dot{\boldsymbol{\varepsilon}}_i$ and $\boldsymbol{\omega}_i$ are obtained by using the SPH approximation of the velocity field in equations (6) and (10) as

$$\begin{aligned} \dot{\boldsymbol{\varepsilon}}_i &= \frac{1}{2}\left(\sum_{j=1}^{N} \frac{m_j}{\rho_j}(\mathbf{v}_j - \mathbf{v}_i)\widetilde{\nabla}W_{ij} + \left(\sum_{j=1}^{N} \frac{m_j}{\rho_j}(\mathbf{v}_j - \mathbf{v}_i)\widetilde{\nabla}W_{ij}\right)^T\right), \\ \boldsymbol{\omega}_i &= \frac{1}{2}\left(\sum_{j=1}^{N} \frac{m_j}{\rho_j}(\mathbf{v}_j - \mathbf{v}_i)\widetilde{\nabla}W_{ij} - \left(\sum_{j=1}^{N} \frac{m_j}{\rho_j}(\mathbf{v}_j - \mathbf{v}_i)\widetilde{\nabla}W_{ij}\right)^T\right), \end{aligned}$$

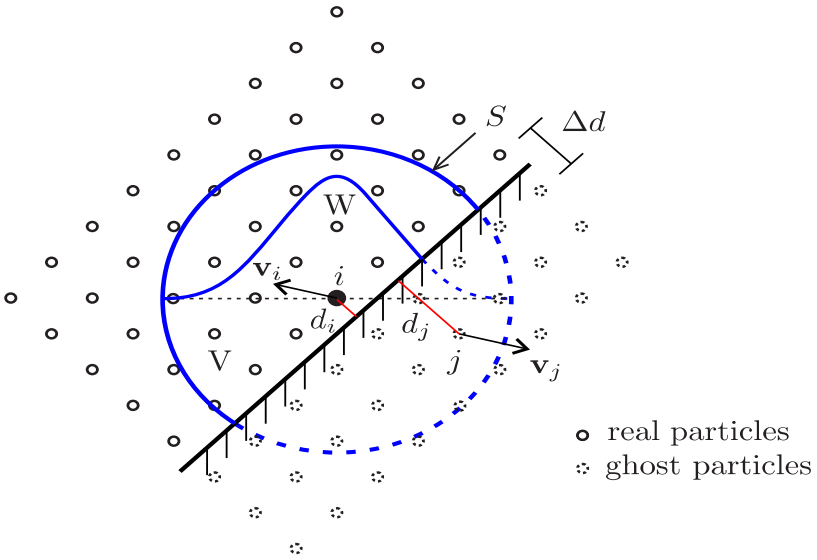

Figure 3: Treatment of boundary conditions using ghost particles in the SPH approximation.

and the approximation of the deviatoric strain rate tensor is computed as $\dot{\boldsymbol{e}}_i = \dot{\boldsymbol{\varepsilon}}_i - \frac{1}{3} tr(\dot{\boldsymbol{\varepsilon}}_i)\mathbf{I}$.

The implementation of boundary conditions for the SPH method is carried out using ideas presented in [24, 29, 30, 36, 5] among others. More precisely, for slip and no-slip boundary conditions in our simulations, we adopt the treatment reported in [5] using ghost particles. Here, we generate three layers of ghost particles outside the solid boundary with a uniform distribution as real particles inside the domain. These particles are located parallel to the solid boundary with the spacing distance $\Delta d/2$ between first layer and solid boundary as shown in Figure 3. The ghost particles will have the same density and mass as the corresponding real particles.

2.2 Artificial viscosity

In many applications in elastodynamics for shock propagation in solids, the numerical solution obtained using the SPH method may present nonphysical oscillations. This is mainly because the transition area for the shock wave does not cover a sufficiently larger length than the particle spacing Δd. As a consequence, the system leads to unstable solutions unless a special treatment is accounted for in the SPH approximation of the governing equations. In this study, to improve the stability of the SPH method and to damp out the nonphysical oscillations, we introduce the artificial viscosity Π_{ij} into the momentum equations as

$$\frac{D\mathbf{v}_i}{Dt} = \sum_{j=1}^{N} m_j \left(\frac{\boldsymbol{\sigma}_j}{\rho_j^2} + \frac{\boldsymbol{\sigma}_i}{\rho_i^2} - \Pi_{ij}\mathbf{I} \right) \widetilde{\nabla} W_{ij}, \tag{16}$$

where the artificial viscosity Π_{ij} is defined as [28]

$$\Pi_{ij} = \begin{cases} \dfrac{-\alpha_\Pi c_{ij}\phi_{ij} + \beta_\Pi \phi_{ij}^2}{\rho_{ij}}, & \text{if} \quad \mathbf{v}_{ij}\cdot\mathbf{r}_{ij} < 0, \\ 0, & \text{if} \quad \mathbf{v}_{ij}\cdot\mathbf{r}_{ij} \geq 0, \end{cases} \tag{17}$$

where $\mathbf{r}_{ij} = |\mathbf{X}_i - \mathbf{X}_j|$ is the distance between the particles i and j, $\mathbf{v}_{ij} = \mathbf{v}_i - \mathbf{v}_j$ is the difference between the velocities of particles i and j, the function ϕ_{ij} is defined by

$$\phi_{ij} = \frac{h_{ij}\mathbf{v}_{ij}\cdot\mathbf{r}_{ij}}{|\mathbf{r}_{ij}|^2 + 0.01h_{ij}^2},$$

with c is the wave speed in the material and it can be calculated as

$$c = \sqrt{\frac{E}{\rho}}. \tag{18}$$

In (17), c_{ij}, ρ_{ij} and h_{ij} are the averaged wave speed, density and smoothing length between the particles defined as

$$c_{ij} = \frac{c_i + c_j}{2}, \qquad \rho_{ij} = \frac{\rho_i + \rho_j}{2}, \qquad h_{ij} = \frac{h_i + h_j}{2}.$$

The coefficients α_Π and β_Π appeared in (17) are used to control the artificial viscosity in the SPH approximation, see for example [28]. Selection of the values for α_Π and β_Π are problem dependent and for the purpose of this study we consider the values $\alpha_\Pi = \beta_\Pi = 2.5$ suggested for SPH simulation of solid mechanics in [19]. Note that the artificial viscosity (17) has been widely used in the literature to improve the numerical stability and prevent the penetration between particles during the compression.

2.3 Tensile instability

For many elsatodynamic problems, the numerical instability in SPH results are more serious for the case under tension than its compression counterpart, see for example [14]. The author in [32] performed the Fourier analysis for turbulence simulations and obtained the conclusion that this instability is caused by the property of the kernel functions. Several techniques have been proposed to overcome this difficulty in the SPH approximation. In [32], another smoothing function is used to avoid particle clumping in the forced turbulence problem using the well-known Wendland kernel. In [10, 11, 31], an approach based on the stress points has also been presented to remove this numerical instability. A total Lagrangian formalism for the SPH method is proposed in [38] to remove the instability. Authors in [25] proposed an artificial repulsive force to prevent neighboring particles clump together under tension. This technique has been improved in [14] by accounting for signs of principal stresses in the artificial repulsive force. This repulsive force is assumed to be increased as two neighboring particles are moving closer. In this work, we consider this later algorithm to deal with the tensile instability in our SPH approximation. Hence, the momentum equation (16) is replaced by

$$\frac{D\mathbf{v}_i}{Dt} = \sum_{j=1}^{N} m_j \left(\frac{\boldsymbol{\sigma}_j}{\rho_j^2} + \frac{\boldsymbol{\sigma}_i}{\rho_i^2} - \Pi_{ij}\mathbf{I} + f_{ij}^n \left(\mathbf{R}_i + \mathbf{R}_j\right) \right) \widetilde{\nabla} W_{ij}, \tag{19}$$

where n is an exponent which dependents on f_{ij} and it is set to $n = 4$ in our simulations as suggested in [25]. The repulsive factor f_{ij} is specified to represent effects of the distance between two neighboring particles and it is defined as

$$f_{ij} = \frac{W_{ij}}{W(\Delta d)}.$$

Note that since Δd is the initial spacing of particles, $W(\Delta d)$ is a constant. The above term ensures that when the distance between two neighboring particles becomes smaller than Δd, the repulsive force term $(\mathbf{R}_i + \mathbf{R}_j)$ turns to be more effective. According to [14], the components of the artificial stresses can be determined by the principal stresses of the corresponding particle. In two-dimensional problems, components of the artificial stresses can be represented by the standard transformations. For instance, the rotation angle θ_i is calculated as

$$\tan\left(2\theta_i\right) = \frac{2\sigma_i^{xy}}{\sigma_i^{xx} - \sigma_i^{yy}}. \tag{20}$$

The stress tensor is transformed into principal stress and its components are expressed as

$$\begin{aligned}\bar{\sigma}_i^{xx} &= \cos^2(\theta_i)\,\sigma_i^{xx} + 2\sin(\theta_i)\cos(\theta_i)\,\sigma_i^{xy} + \sin^2(\theta_i)\,\sigma_i^{yy},\\ \bar{\sigma}_i^{yy} &= \sin^2(\theta_i)\,\sigma_i^{xx} - 2\sin(\theta_i)\cos(\theta_i)\,\sigma_i^{xy} + \cos^2(\theta_i)\,\sigma_i^{yy}.\end{aligned} \tag{21}$$

The principal stress is also applied to identify the diagonal components of the artificial stress as

$$\bar{R}_i^{xx} = \begin{cases} -\epsilon\dfrac{\bar{\sigma}_i^{xx}}{\rho_i^2}, & \text{if} \quad \bar{\sigma}_i^{xx} > 0,\\ \\ 0, & \text{if} \quad \bar{\sigma}_i^{xx} \leq 0, \end{cases} \tag{22}$$

where ϵ is a parameter with values in $[0,1]$ and the minus sign in (22) is used to cancel part of the stress in the case of tension (here $\sigma_i^{xx} > 0$ indicate the state of tension). As suggested in [14] for solid mechanics, we use $\epsilon = 0.3$ in the numerical results presented in this study. The remaining term $\bar{R}_i^{yy}$ can be simply calculated by changing the subscript xx by yy in the equation (22). Finally, to transform the diagonal components of the artificial stress to the original coordinates we use

$$\begin{aligned}R_i^{xx} &= \bar{R}_i^{xx}\cos^2(\theta_i) + \bar{R}_i^{yy}\sin^2(\theta_i),\\ R_i^{yy} &= \bar{R}_i^{xx}\sin^2(\theta_i) + \bar{R}_i^{yy}\cos^2(\theta_i),\\ R_i^{xy} &= (\bar{R}_i^{xx} - \bar{R}_i^{yy})\sin(\theta_i)\cos(\theta_i).\end{aligned} \tag{23}$$

The term $\mathbf{R}_j$ can be calculated in a similar manner by replacing the subscript i with j in the equations (20)-(23). Note that this approach only becomes effective when the particles clump together under tension.

3 Runge-Kutta Chebyshev scheme

The solution procedure for equations (5) is complete when a time integration of the semi-discrete SPH equations is selected. This stage can be handled by any implicit ODE solver, since they are computationally without risk by virtue of their accuracy and unconditionally stability. This allows for larger timesteps in the integration process. However, due to the large set of linear systems of algebraic equations at each timestep, these methods may be computationally inefficient. As an alternative, we use a class of explicit Runge-Kutta methods. Applied to the system (5), the SPH discretization can be reformulated in a compact system of ODEs as

$$\frac{D\mathbf{U}}{Dt} = \mathbf{F}(t,\mathbf{U}), \qquad t \in (0,T], \tag{24}$$

where $\mathbf{U} = (\mathrm{v}^x, \mathrm{v}^y, \sigma^{xx}, \sigma^{yy}, \sigma^{xy}, r^x, r^y)^T$, the right-hand side function $\mathbf{F}(t,\mathbf{U})$ is defined for each particle i by

$$\begin{pmatrix}
\displaystyle\sum_{j=1}^{N} m_j\Big(\frac{\sigma_j^{xx}}{\rho_j^2} + \frac{\sigma_i^{xx}}{\rho_i^2} - \Pi_{ij}^{xx} + f_{ij}^n(R_i^{xx} + R_j^{xx})\Big)\frac{\partial\widetilde{W}_{ij}}{\partial x} + \sum_{j=1}^{N} m_j\Big(\frac{\sigma_j^{xy}}{\rho_j^2} + \frac{\sigma_i^{xy}}{\rho_i^2} + f_{ij}^n(R_i^{xy} + R_j^{xy})\Big)\frac{\partial\widetilde{W}_{ij}}{\partial y}\\
\displaystyle\sum_{j=1}^{N} m_j\Big(\frac{\sigma_j^{yx}}{\rho_j^2} + \frac{\sigma_i^{yx}}{\rho_i^2} + f_{ij}^n(R_i^{yx} + R_j^{yx})\Big)\frac{\partial\widetilde{W}_{ij}}{\partial x} + \sum_{j=1}^{N} m_j\Big(\frac{\sigma_j^{yy}}{\rho_j^2} + \frac{\sigma_i^{yy}}{\rho_i^2} - \Pi_{ij}^{yy} + f_{ij}^n(R_i^{yy} + R_j^{yy})\Big)\frac{\partial\widetilde{W}_{ij}}{\partial y}\\
\displaystyle\sum_{j=1}^{N}\frac{m_j}{\rho_j}\Big(D_{11}\mathrm{v}_j^x - D_{11}\mathrm{v}_i^x\Big)\frac{\partial\widetilde{W}_{ij}}{\partial x} + \sum_{j=1}^{N}\frac{m_j}{\rho_j}\Big(D_{12}\mathrm{v}_j^y - D_{12}\mathrm{v}_i^y\Big)\frac{\partial\widetilde{W}_{ij}}{\partial y}\\
\displaystyle\sum_{j=1}^{N}\frac{m_j}{\rho_j}\Big(D_{21}\mathrm{v}_j^x - D_{21}\mathrm{v}_i^x\Big)\frac{\partial\widetilde{W}_{ij}}{\partial x} + \sum_{j=1}^{N}\frac{m_j}{\rho_j}\Big(D_{22}\mathrm{v}_j^y - D_{22}\mathrm{v}_i^y\Big)\frac{\partial\widetilde{W}_{ij}}{\partial y}\\
\displaystyle\sum_{j=1}^{N}\frac{m_j}{\rho_j}\Big(D_{33}\mathrm{v}_j^y - D_{33}\mathrm{v}_i^y\Big)\frac{\partial\widetilde{W}_{ij}}{\partial x} + \sum_{j=1}^{N}\frac{m_j}{\rho_j}\Big(D_{33}\mathrm{v}_j^x - D_{33}\mathrm{v}_i^x\Big)\frac{\partial\widetilde{W}_{ij}}{\partial y}\\
\mathrm{v}_i^x\\
\mathrm{v}_i^y
\end{pmatrix},$$

with D_{ij} are the entries of the elastic matrix $\mathbf{D}$ for plane stress *i.e.*,

$$\mathbf{D} = \frac{E}{(1-\nu^2)} \begin{pmatrix} 1 & \nu & 0 \\ \nu & 1 & 0 \\ 0 & 0 & \dfrac{1-\nu}{2} \end{pmatrix}.$$

To integrate the equations (24) we divide the time interval into subintervals $[t_n, t_{n+1}]$ with duration $\Delta t = t_{n+1} - t_n$ for $n = 0, 1, \ldots$. We use the notation w^n to denote the value of a generic function w at time t_n.

Difficulties often appear when the Jacobian of $\mathbf{F}$, $\partial\mathbf{F}/\partial\mathbf{U}$, has large eigenvalues. This may give rise to numerical stiffness. Thus, time integration schemes for (24) depend strongly on the spectral radius $\rho\,(\partial\mathbf{F}/\partial\mathbf{U})$, and for these reasons it is preferable that these schemes have to be either implicit or explicit with large stability regions. In the current work, we consider the Runge-Kutta Chebyshev (RKC) method studied in many references, see for example [7, 37, 8]. To solve the system (24), the RKC scheme takes the form

$$\begin{aligned} \mathbf{U}^{(0)} &= \tilde{\mathbf{U}}^n\,, \\ \mathbf{U}^{(1)} &= \mathbf{U}^{(0)} + \tilde{\mu}_1 \mathbf{F}^{(0)} \\ \mathbf{U}^{(j)} &= \mu_j \mathbf{U}^{(j-1)} + \nu_j \mathbf{U}^{(j-2)} + (1-\mu_j-\nu_j)\mathbf{U}^{(0)} + \tilde{\mu}_j \mathbf{F}^{(j-1)} + \tilde{\gamma}_j \mathbf{F}^{(0)}, \qquad 2 \le j \le s\,, \\ \mathbf{U}^{n+1} &= \mathbf{U}^{(s)}\,, \end{aligned} \tag{25}$$

where $\tilde{\mathbf{U}}^n$ is the solution computed from the Lagrangian fractional step, $\mathbf{F}^{(j)}$ denotes the term $\mathbf{F}\left(t_n + c_j\Delta t, \mathbf{U}^{(j)}\right)$ and $\mathbf{U}^{(j)}$ are internal vectors for RKC stages. The coefficients in (25) are available in analytical form for arbitrary s from [7, 37]. For convenience of the reader we include the formulas for these coefficients. Consider the Chebyshev polynomial of the first kind of degree j

$$T_j(z) = \cos(j \arccos z), \qquad -1 \le z \le 1\,.$$

Then,

$$\epsilon = \frac{2}{13}, \qquad q_0 = 1 + \frac{\epsilon}{s^2}, \qquad q_1 = \frac{T_s'(q_0)}{T_s''(q_0)}\,,$$

$$b_j = \frac{T_j''(q_0)}{(T_j'(q_0))^2}, \qquad (2 \le j \le s), \qquad b_0 = b_2, \quad b_1 = b_2\,,$$

and

$$\tilde{\mu}_1 = b_1 q_1, \qquad \mu_j = 2q_0 \frac{b_j}{b_{j-1}}, \qquad \nu_j = -\frac{b_j}{b_{j-2}}, \qquad \tilde{\mu}_j = 2q_1 \frac{b_j}{b_{j-1}}\,,$$

$$\tilde{\gamma}_j = (1 - b_{j-1} T_{j-1}(q_0))\tilde{\mu}_j, \qquad (2 \le j \le s)\,.$$

The coefficients c_j are

$$c_j = \frac{T_s'(q_0)}{T_s''(q_0)} \frac{T_j''(q_0)}{T_j'(q_0)} \approx \frac{j^2-1}{s^2-1} \quad (2 \le j \le s), \qquad c_1 = \frac{c_2}{T_2'(q_0)} \approx \frac{c_2}{4}, \qquad c_s = 1\,.$$

It should be pointed out that two criteria have been taken into consideration for the calculation of the above coefficients namely, (i) the real stability boundary has to be as large as possible to obtain good stability properties for the problem under study, and (ii) the application of the method with arbitrary number of stages should not damage the convergence properties, that is, the accumulation

of local errors does not grow without bound. Thus, the number of stages s in our SPH method and the conventional RKC scheme varies with Δt such that, see [37],

$$s = 1 + \left[\!\left[\sqrt{1 + \frac{\rho\,(\partial \mathbf{F}/\partial \mathbf{U})}{0.653}} \right]\!\right], \tag{26}$$

where $[\![\, x \,]\!]$ denotes the integer part of x. In our case, an upper bound for $\rho\,(\partial \mathbf{F}/\partial \mathbf{U})$ is estimated once and for all by using Gerschgorin theorem and the relation (26) is replaced by

$$s = 1 + \left[\!\left[\sqrt{1 + \frac{c\Delta t}{0.131\Delta d}} \right]\!\right], \tag{27}$$

where c is the wave speed in the material defined by (18) and Δd is the initial spacing of particles in the computational domain.

4 Numerical results and examples

To demonstrate the performance of the proposed SPH method, several examples are presented. For the first example, an exact solution is readily available which makes it ideal for a quantitative as well as qualitative validation of the considered SPH method. We also compare numerical results obtained using different time stepping schemes in SPH method for this example. As a second example we consider an oscillatory beam and in the third example we simulate elastic plate with a void. For all these examples the material is assumed to be Magnesium with density $\rho = 1738\ kg/m^3$, Young's modulus $E = 45 \times 10^9\ Pa$ and Poisson ratio $\nu = 0.35$. In line with hyperbolic systems of conservation laws we also define the CFL number as

$$\mathrm{CFL} = c\frac{\Delta t}{\Delta d},$$

and the equation (26) becomes

$$s = 1 + \left[\!\left[\sqrt{1 + \frac{\mathrm{CFL}}{0.131}} \right]\!\right]. \tag{28}$$

In all the computations reported herein, the CFL is set to a given value and the number of stages s in the RKC scheme is adjusted according to the condition (28). The aim is to show that, using reasonably low number of particles and large CFL values, the proposed method reproduces the corresponding elastodynamic patterns and accurately captures the deformation structures with little numerical diffusion, even after long time simulations.

4.1 Shock wave problem

In this example, we solve the propagation problem of a shock wave in a Magnesium bar with a length of $L = 1\ m$. Initially the bar is at rest with the right end of the bar is fixed while a compression stress is applied on the left boundary using a stress $\sigma_0 = 8.8436 \times 10^6\ Pa$. The analytical velocity of the shock wave in this problem can easily be calculated as $\mathrm{v}_0 = \sigma_0/\sqrt{E\rho} = 1\ m/s$. The wave propagates along the bar with the speed $c = \sqrt{E/\rho} = 5.0884 \times 10^3\ m/s$ and when the wave arrives at the fixed right end of the bar, the stress at this point becomes $17.6872 \times 10^6\ Pa$. Since the analytical solution is known, we evaluate the error function $\mathcal{E}^n$ at time t_n for any generic function W as

$$\mathcal{E}_i^n = W^{Exact}(\mathbf{X}_i, t_n) - W_i^n,$$

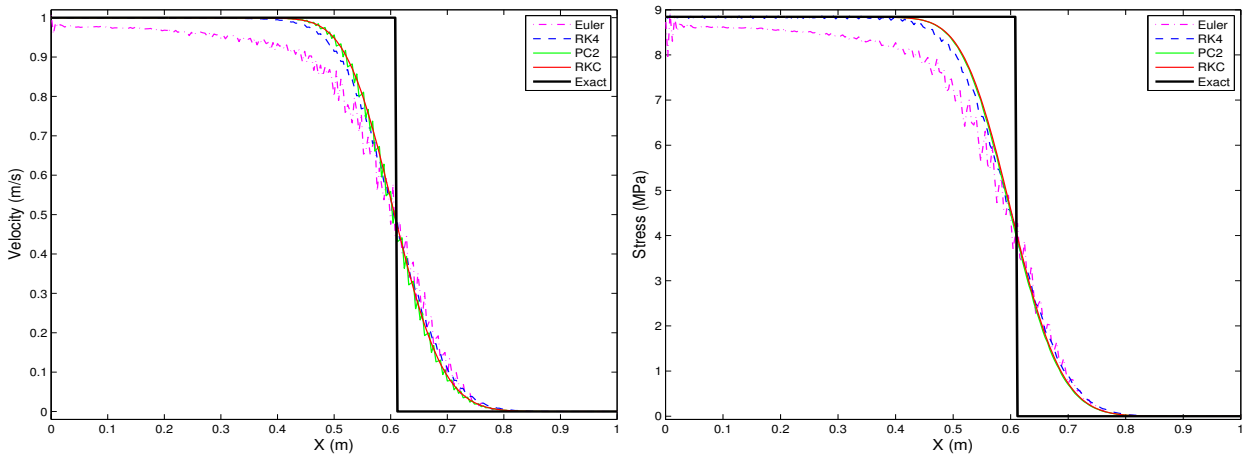

Figure 4: Velocity (left) and stress (right) profiles along the bar at $t = 0.12\ ms$ using different time stepping schemes.

where W^{Exact} and W_i^n are the analytical and numerical solutions respectively, evaluated at the particle i and time t_n. The aim of this test example is to assess the performance of the proposed RKC scheme, the conventional explicit Euler scheme, the classical fourth-order explicit Runge-Kutta (RK4) scheme and a second-order predictor-corrector (PC2) scheme in the SPH method. The Euler and RK4 schemes have been widely used in the literature and their formulations to solve the ODE system (24) are straightforward. The PC2 scheme has also been applied in conjunction with SPH method to solve problems in both fluid dynamics and solid mechanics, see for example [13, 27]. Its formulation to solve the system (24) can be carried out as

$$\begin{aligned} \mathbf{U}^{n+\frac{1}{2}} &= \mathbf{U}^n + \frac{1}{2}\Delta t \mathbf{F}\left(t_n, \mathbf{U}^n\right), \\ \widehat{\mathbf{U}}^{n+\frac{1}{2}} &= \mathbf{U}^n + \frac{1}{2}\Delta t \mathbf{F}\left(t_n + \frac{\Delta t}{2}, \mathbf{U}^{n+\frac{1}{2}}\right), \\ \mathbf{U}^{n+1} &= 2\widehat{\mathbf{U}}^{n+\frac{1}{2}} - \mathbf{U}^n. \end{aligned} \tag{29}$$

In Figure 4 we display the profiles of velocity and stress solutions along the bar at $t = 0.12\ ms$ using a collocation set of 250 particles and CFL $= 0.6$ for the considered time stepping schemes. The time evolution of velocity and stress solutions at the mid point ($x = \frac{L}{2}$) of the bar is shown in Figure 5. It is clear from these results that both the Euler and PC2 schemes exhibit oscillatory behavior for the SPH solution of the velocity field. On the other hand the results obtained using the RK4 and RKC schemes are similar and no oscillations have been detected in their solutions. However, the RK4 scheme requires about the double of computational work compared to the RKC scheme. Note that for the considered CFL value, the RKC scheme uses only two stages whereas four stages are needed in the RK4 scheme. It should also be pointed out that for CFL > 0.6 the Euler and PC2 schemes become unstable and the RK4 scheme becomes unstable for CFL > 1.2. This is not the case for the RKC scheme as the results remain stable independently of the CFL in this test problem. To further examine the effect of CFL on these schemes we present in Figure 6 the velocity and stress profiles along the bar and in Figure 7 the time evolution of velocity and stress solutions at the mid point of the bar using different values of CFL in both RK4 and RKC schemes. Increasing the CFL in the RK4 scheme results in an increase of the numerical dissipation and for CFL $= 1$ oscillations start to appear in the results. On the other hand, results obtained using the RKC scheme remain stable independently from the values taken by CFL. No deterioration in the accuracy has been detected in the numerical results obtained using the RKC scheme.

Table 1: Results for the shock wave problem at $t = 0.12\ ms$ using different numbers of particles and different timesteps in the considered time stepping schemes. The CPU times are given in seconds and the number between brackets refers to the number of stages in RKC scheme.

		$\Delta t = 11.8\ \mu s$				$\Delta t = 23.6\ \mu s$				$\Delta t = 47.2\ \mu s$			
NP		Euler	PC2	RK4	RKC	Euler	PC2	RK4	RKC	Euler	PC2	RK4	RKC
	L^1-error	0.0840	0.0889	0.0889	0.0889	0.0789	0.0889	0.0889	0.0889	0.1469	0.0886	0.1005	0.0889
250	L^2-error	0.1569	0.1613	0.1613	0.1613	0.1519	0.1613	0.1613	0.1613	0.1943	0.1613	0.171	0.1612
	CPU	97.6	259.8	558.9	276.3(2)	49.9	111.7	279.8	159.3(2)	32.2	66.6	108.1	95.7(3)
	L^1-error	0.0555	0.0625	0.0625	0.0625	0.1002	0.0625	0.0626	0.0625	—	—	0.1764	0.0643
500	L^2-error	0.1275	0.1353	0.1353	0.1353	0.1598	0.1354	0.1354	0.1354	—	—	0.2172	0.01372
	CPU	131.5	326.3	674.3	351.8(2)	61.6	195.8	315.2	288.3(3)	—	—	178.5	146.2(4)
	L^1-error	0.0480	0.0510	0.0510	0.0511	—	—	0.0618	0.051	—	—	—	0.0522
750	L^2-error	0.1180	0.1221	0.1221	0.1222	—	—	0.134	0.1221	—	—	—	0.1234
	CPU	151.5	417.6	790.6	434.6(2)	—	—	390.7	334.4(3)	—	—	—	229.4(4)
	L^1-error	0.0675	0.0441	0.0441	0.0441	—	—	0.1203	0.0445	—	—	—	0.0441
1000	L^2-error	0.1323	0.1137	0.1136	0.1136	—	—	0.1797	0.1153	—	—	—	0.1137
	CPU	231.5	470.7	896.7	738.6(3)	—	—	445.0	381.1(4)	—	—	—	323.7(5)

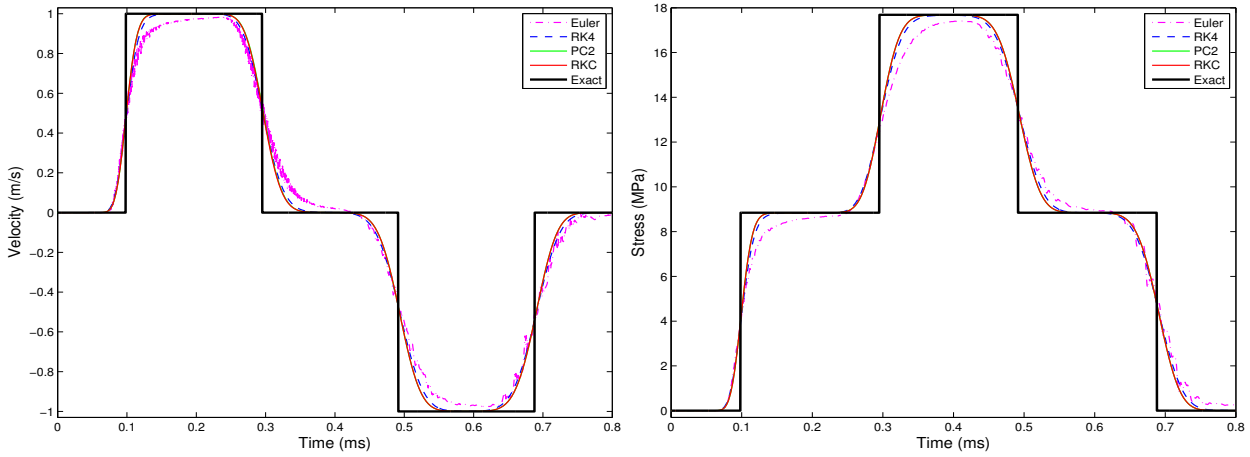

Figure 5: Time evolution of velocity (left) and stress (right) for the shock wave problem at the mid point of the bar using different time stepping schemes.

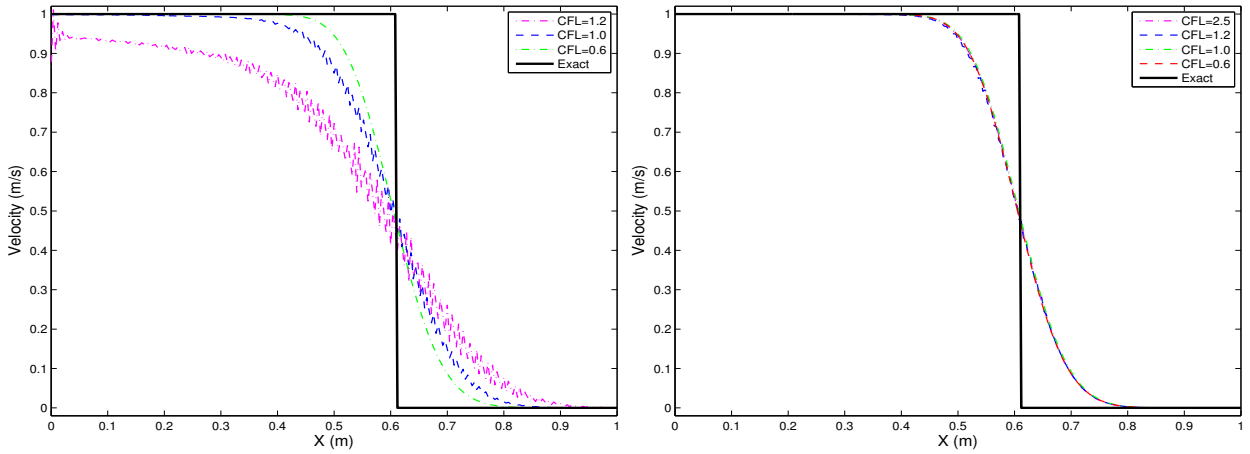

Figure 6: Velocity profile along the bar at $t = 0.12\ ms$ using RK4 (left) and RKC (right) using different values of CFL.

Next we examine the performance of RKC method using different numbers of particles in the bar. To this end we display in Figure 8 the velocity and stress profiles along the bar and in Figure 9 the time evolution of velocity and stress solutions at the mid point of the bar using three different numbers of particles (NP) and a fixed CFL = 2.5. It is clear from these results that using large number of particles in the simulation yields improved results with a noticeable reduction in the numerical dissipation. Note that these results are obtained using a fixed timestep (calculated from the definition of CFL) while the number of stages in RKC scheme varies according to the equation (28). To quantify these results we summarize in Table 1 the L^1- and L^2-error norms for the time stepping schemes considered in this study using different numbers of particles and different timesteps. In this table we also include computational cost referred to by the CPU time associated with each time stepping scheme. Examination of Table 1 shows that for low number of particles and small timesteps the three schemes give roughly similar results with differences in the CPU time. However, by increasing the number of particles or the value of timesteps, the results obtained using by RKC scheme are slightly more accurate and efficient than results obtained by PC2 and RK4 schemes, respectively. With increasing the number of particles or the value of timesteps, the

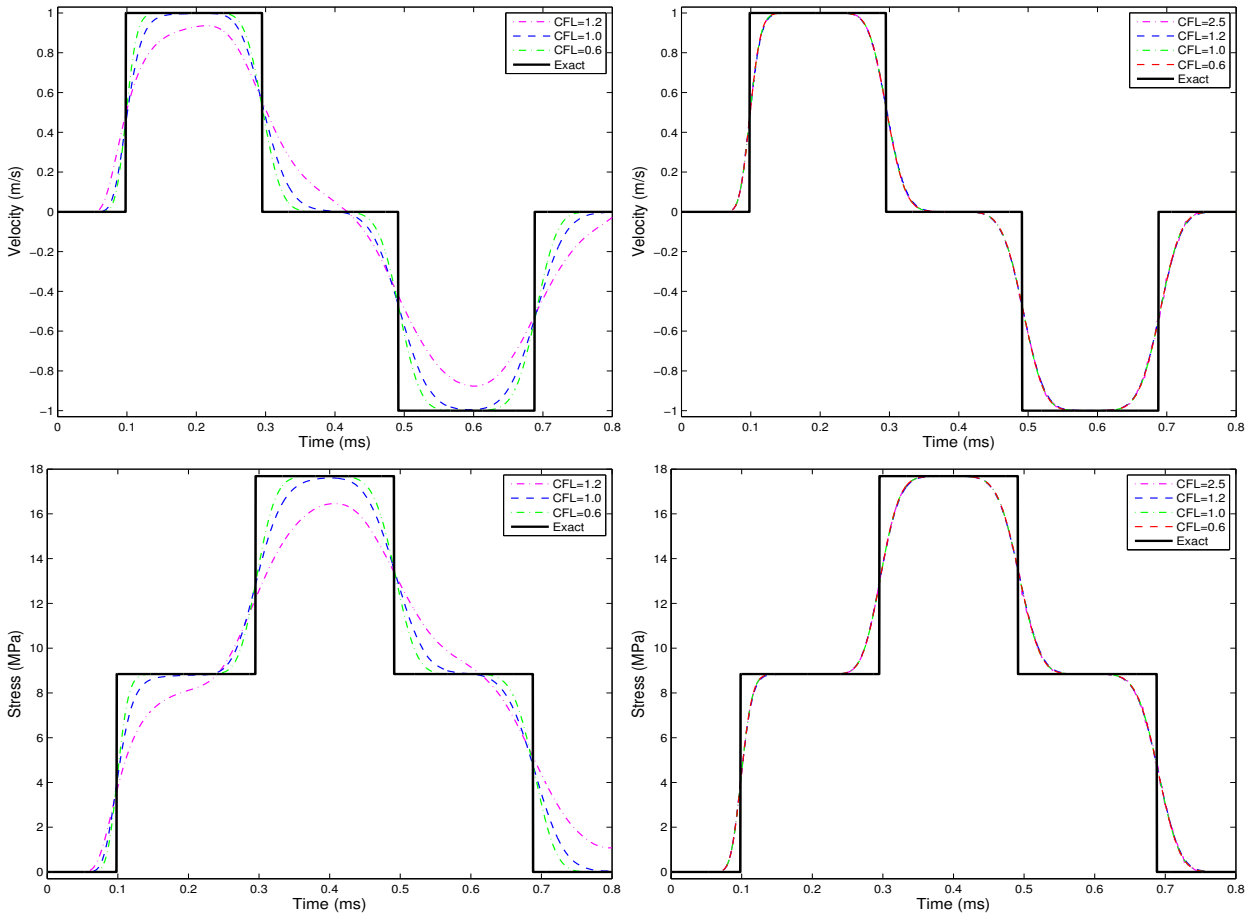

Figure 7: Time evolution of stress and velocity for the shock wave problem at the mid point of the bar using RK4 (left column) and RKC (right column).

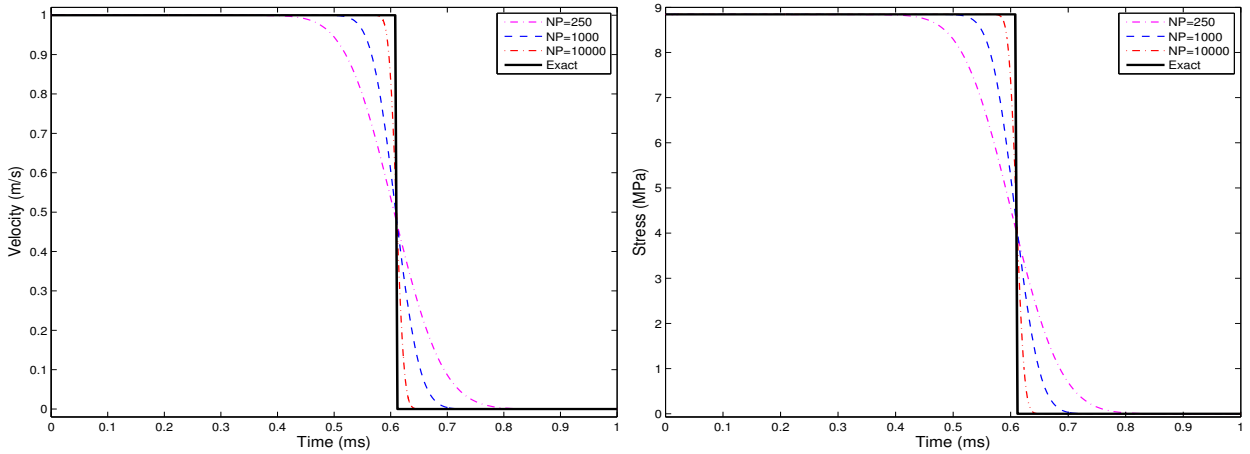

Figure 8: Velocity (left) and stress (right) profiles along the bar at $t = 0.12\ ms$ using RKC method with different numbers of particles.

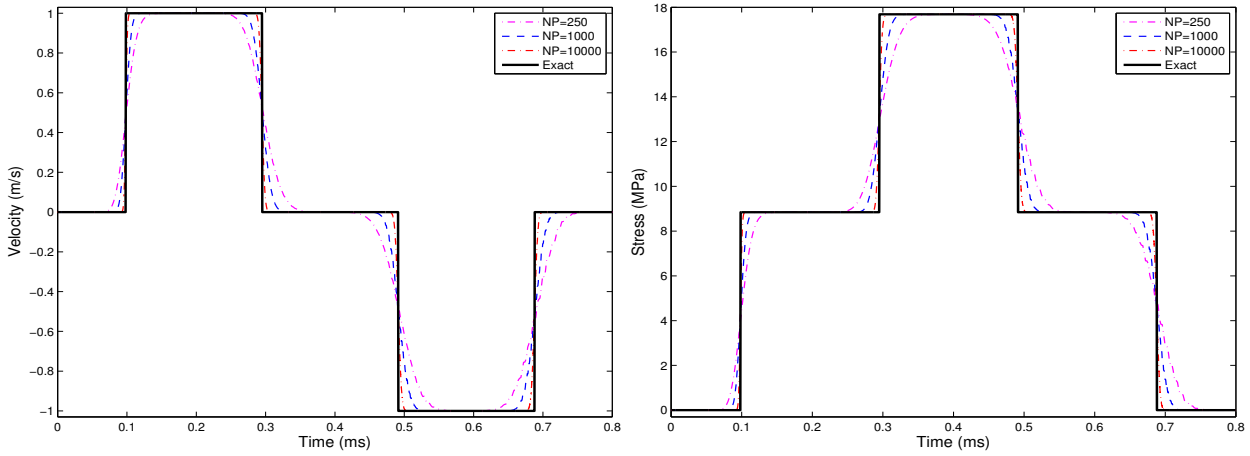

Figure 9: Time evolution of velocity (left) and stress (right) for the shock wave problem at the mid point of the bar using RKC method with different numbers of particles.

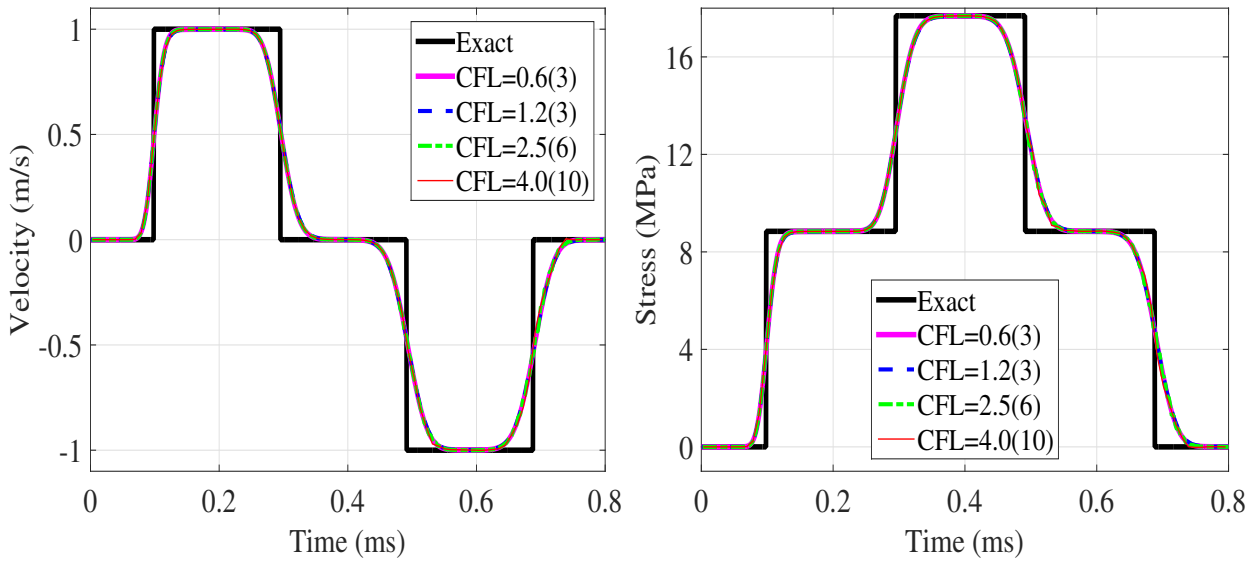

Figure 10: Time evolution of velocity (left) and stress (right) for the shock wave problem at the mid point of the bar using RKC method with different values of CFL and a fixed limit for number of stages.

PC2 and RK4 schemes go unstable (— in Table 1 corresponds to runs where the PC2 and RK4 schemes become unstable). It is worth remarking that for large numbers of particles or low values of timesteps the CPU time in the RKC scheme becomes larger. For example, in a run with NP = 1000 and $\Delta t = 11.8\ \mu s$ the CPU time spent to perform a RKC step is more than twice that of a RKC step using NP = 250 and $\Delta t = 11.8\ \mu s$. However, the same accuracy can be achieved by RKC scheme with NP = 1000 and $\Delta t = 47.2\ \mu s$ at low computational cost. Finally, we set a limit to the number of stages as $s = 10$ and we perform the same simulations using different values for CFL. The obtained results for the time evolution of velocity and stress solutions at the mid point of the bar are presented in Figure 10. It is clear from this figure that the computed results do not depend on the number of stages used in the RKC scheme and for a fixed bound for this number the proposed method still produces stable results with large values of CFL. As can be seen from the solutions displayed in the above figures and the errors presented in Table 1, high accuracy is achieved in the SPH method with RKC scheme for this test example in terms of the considered error norms. Hence, our next computations are realized using only the SPH-RKC scheme.

4.2 Oscillatory beam problem

This example solves a problem of oscillatory thin beam made of Magnesium with length and wide denoted by L and W, respectively. The left end of the beam is fixed, the other end is free and a perpendicular velocity v_y is loaded on the beam at the initial time [14]. The purpose of this test example is to examine the performance of the proposed SPH method for solving elastodynamic problems in presence of large deformation. Here, the velocity v_y at each point on the beam is calculated from

$$\frac{\mathrm{v}_y}{c} = V_f \frac{M\Big(\cos(\kappa x) - \cosh(\kappa x)\Big) - N\Big(\sin(\kappa x) - \sinh(\kappa x)\Big)}{Q}, \tag{30}$$

where c is the wave speed of the material, V_f is a factor used to control the magnitude of velocity, and κ is a factor assumed to satisfy the condition

$$\cos(\kappa L)\cosh(\kappa L) = -1.$$

It is easy to verify that for this mode $\kappa L = 1.875$, and the other factors in (30) are calculated as

$$\begin{aligned} M &= \sin(\kappa L) + \sinh(\kappa L), \\ N &= \cos(\kappa L) + \cosh(\kappa L), \\ Q &= 2\Big(\cos(\kappa L)\sinh(\kappa L) - \sin(\kappa L)\cosh(\kappa L)\Big). \end{aligned}$$

For this oscillatory beam problem, the equation of frequency ω is given by [18]

$$\omega = \sqrt{\frac{EW^2\kappa^4}{12\rho}}. \tag{31}$$

In the first run with this example we set $L = 0.5\ m$, $W = 0.05\ m$, $V_f = 0.02$ and a set of particles uniformly distributed along the beam with initial spacing $\Delta d = 0.0033\ m$ are used in our simulation. Figure 11 and Figure 12 present the distribution of the principal stress fields σ^{11} and σ^{22}, respectively. The results are presented for four different times $t = 73.7\ \mu s$, $1621.33\ \mu s$, $3316.37\ \mu s$ and $4937.7\ \mu s$ using a fixed CFL = 2.5. Note that for this value of CFL, the explicit schemes considered in the previous example are unstable and therefore can not be used to solve this problem whereas the RKC scheme is stable and it requires only five stages for the solution of

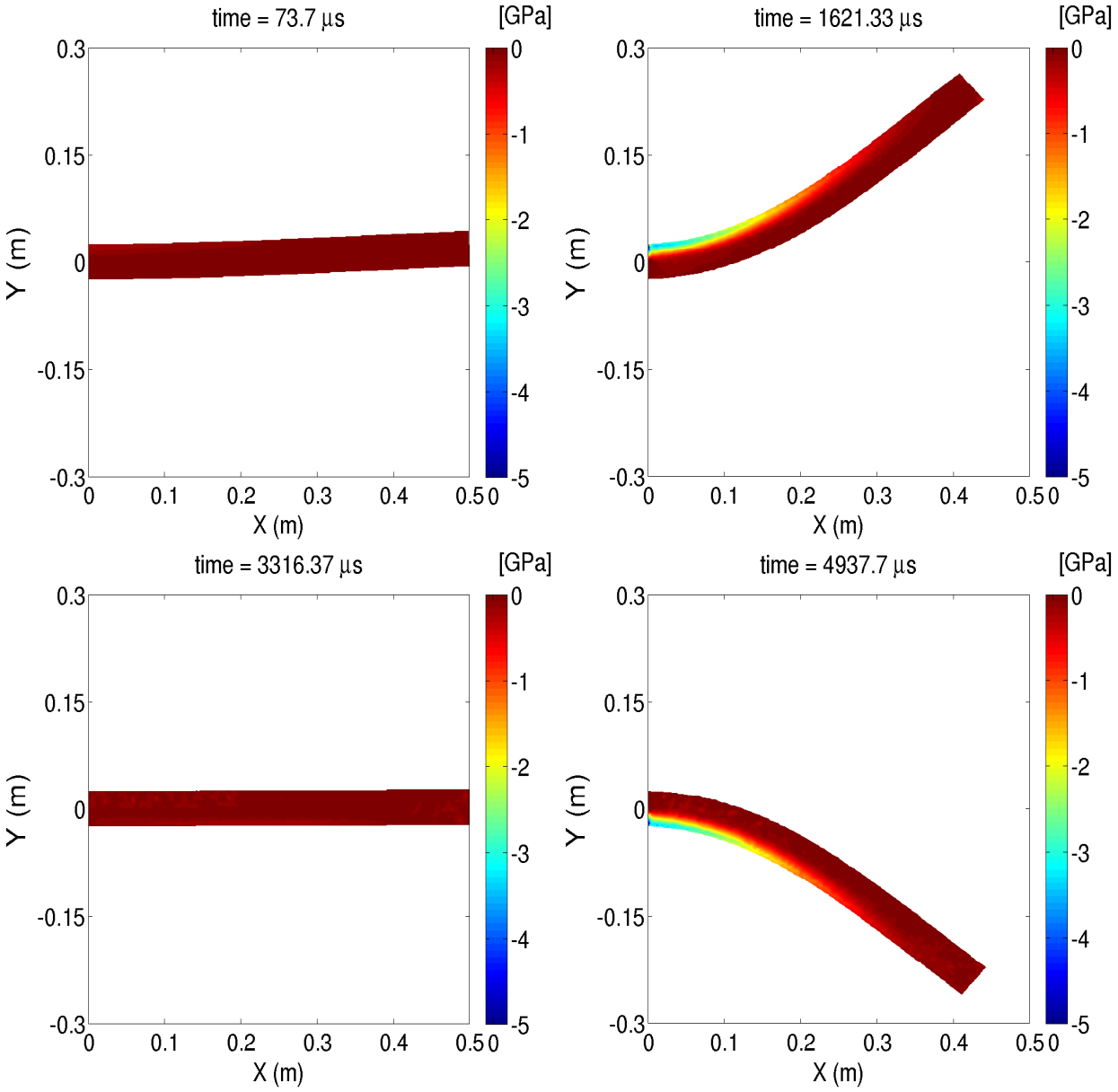

Figure 11: Distribution of the principal stress field σ^{11} for the oscillatory beam problem using SPH-RKC method at four different instants.

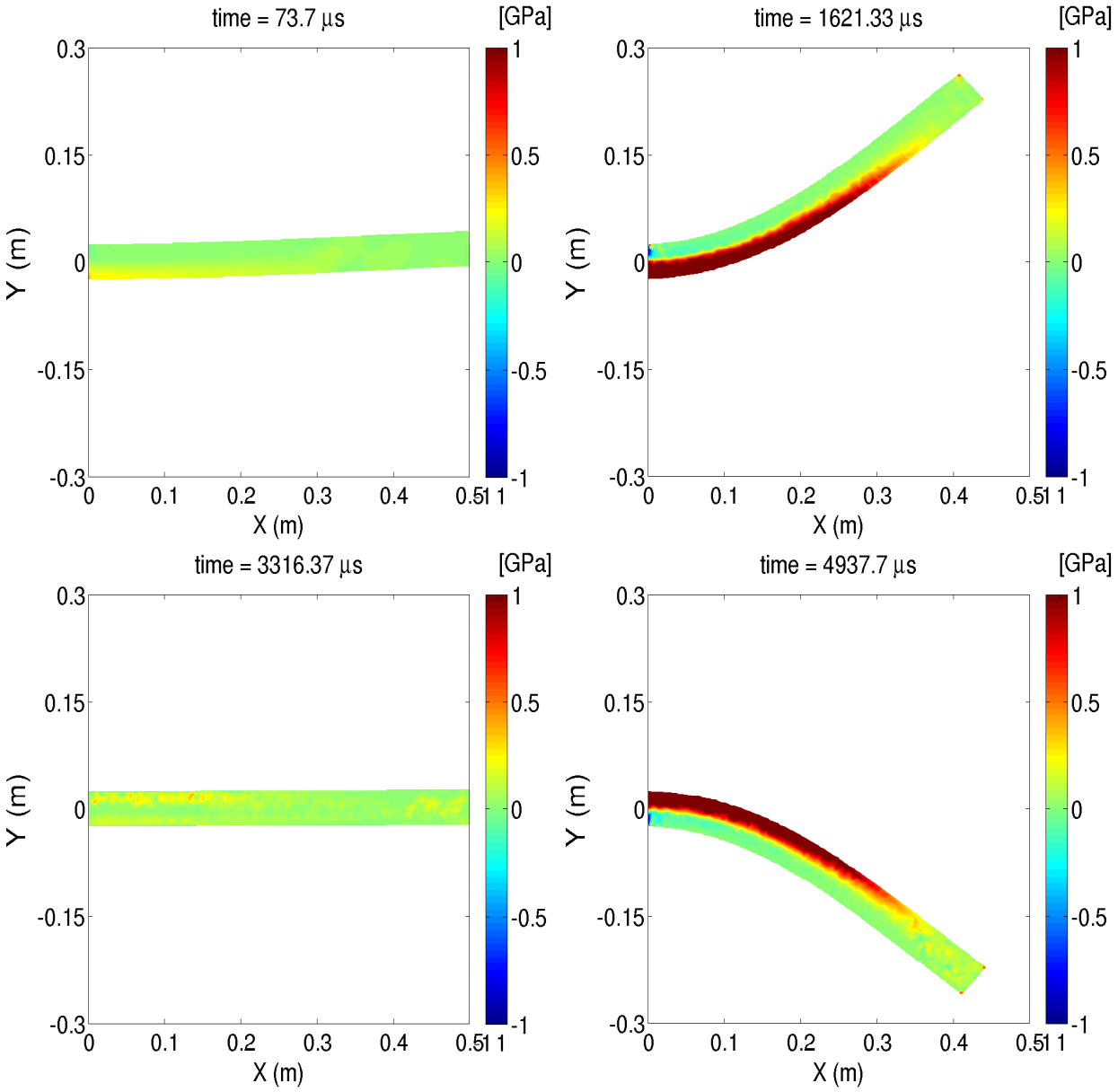

Figure 12: Distribution of the principal stress field σ^{22} for the oscillatory beam problem using SPH-RKC method at four different instants.

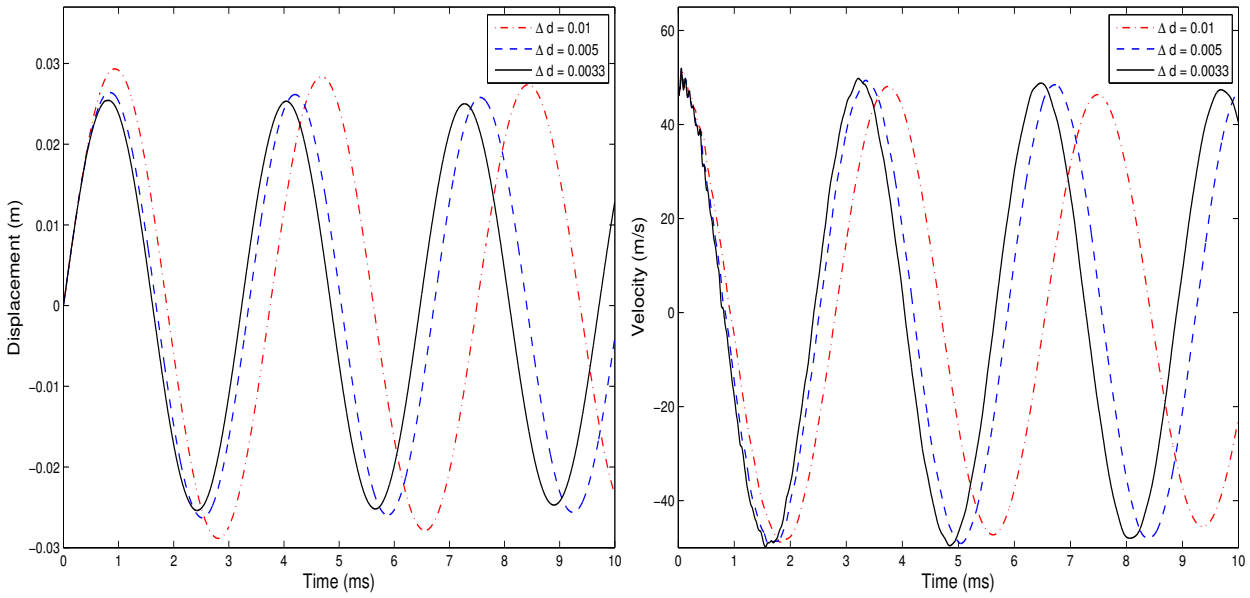

Figure 13: Time evolution of displacement (left) and velocity (right) at the end of the beam with different numbers of particles for the oscillatory beam problem using $L = 0.5\ m$ and $W = 0.1\ m$.

this problem. It is clear that no oscillations or smearing of the deformation have been detected in the computed results. As can be seen, good behavior is recovered by the proposed SPH-RKC method for the considered elastodynamic conditions without any significant loss of accuracy. The performance of the proposed SPH-RKC method is very attractive since the computed solutions remain stable and accurate even for relatively coarse particle distributions without requiring small timesteps for the stability of the explicit time stepping scheme.

To examine the effect of number of particles on the results for this example we plot in Figure 13 the time evolution of the displacement and velocity at the end of the beam using three sets of particles with initial spacing $\Delta d = 0.01\ m$, $0.005\ m$ and $0.0033\ m$. It is evident that, increasing the number of particles in the simulation, the convergence is achieved in our SPH-RKC method for this test example. A better resolution is obtained for larger number of particles and once this number reaches a limit of $\Delta d = 0.0033\ m$ the improvement in the results becomes minimal but at higher computational cost. It should also be noted that for the results presented in this figure the time step Δt remains constant and the number of stages in RKC scheme is $s = 3$, 4 and 5 for $\Delta d = 0.01\ m$, $0.005\ m$ and $0.0033\ m$, respectively. On the other hand, refining the number of particles keeping constant the timestep, the considered Euler, PC2 and RK4 schemes yield spurious oscillations and become unstable at the end.

To ascertain the quality of the resolution of SPH-RKC method for this example, we compare in Table 2 the computed frequency to the theoretical frequency given by (31) using $\Delta d = 0.0033\ m$. We consider two values for the beam width W and several values for the factor V_f to assess the performance of the proposed SPH-RKC method to accurately capture the oscillatory behavior of the beam. As can be seen, more accurate results are obtained for a beam with $W = 0.05\ m$ than for the case with $W = 0.1\ m$. The errors also decrease as the factor V_f becomes smaller and in all cases the error is less than 9% for the case with $W = 0.1\ m$ and less than 5% for the other case with $W = 0.05\ m$. The computed solutions using the proposed SPH-RKC method seem to converge to the physically relevant solutions in all selected test cases. The proposed SPH-RKC method captures the elastic deformation accurately, does not diffuse the stress fields or give nonphysical oscillations near the steep gradients.

Table 2: Comparison results for the frequency using different values of V_f in the oscillatory beam problem.

	$W = 0.1\ m$			$W = 0.05\ m$		
V_f	$\omega_{\text{theoretical}}$	ω_{SPH}	error	$\omega_{\text{theoretical}}$	ω_{SPH}	error
0.05	2066 Hz	1888 Hz	8.62%	1033 Hz	982 Hz	4.94%
0.02	2066 Hz	1929 Hz	6.63%	1033 Hz	983 Hz	4.84%
0.01	2066 Hz	1943 Hz	5.95%	1033 Hz	1000 Hz	3.19%
0.005	2066 Hz	1943 Hz	5.95%	1033 Hz	1007 Hz	2.52%
0.002	2066 Hz	1943 Hz	5.95%	1033 Hz	1007 Hz	2.52%
0.001	2066 Hz	1943 Hz	5.95%	1033 Hz	1007 Hz	2.52%

4.3 Elastic plate problem with a void

Our final test example consists of an elastic plate with a void under compression. The material is Magnesium and the plate is assumed to be squared with length $L = 2\ m$ including a circular void with radius $R_0 = 0.3\ m$, see Figure 14. A fixed velocity of $0.2\ m/s$ is applied on the top and bottom boundaries of the plate and the remaining boundaries are kept free. Note that because of the symmetry in this problem it is more efficient to consider only quarter of the computational domain. The aim of this test example is to examine the performance of the proposed SPH-RKC method to resolve complex stress features and to preserve the symmetry in the numerical solutions. In addition, since the SPH-RKC method is a particle-based method, the distribution of particles would influence the accuracy of its analysis. To illustrate this effect we consider three collocation sets of particles namely squared distribution, radial distribution and equally radial distribution as depicted in Figure 15. For a better insight, only a coarser view is illustrated in this figure. The total number of particles for each collocation set is 897, 922 and 916 for the squared distribution, the radial distribution and the equally radial distribution, respectively. In all our simulations for this problem we use a fixed CFL = 2.5 and for this value of CFL we have found that the number of stages in the RKC scheme does not overpass six stages.

Figure 16 presents the normal stresses σ^{xy} and σ^{yy}, and the velocity field obtained on each collocation set at time $t = 994.9097\ ms$. As can be seen from these results, both squared and radial distributions exhibit nonphysical oscillations in the stress patterns. The results obtained on the squared distribution also produce cracking effects on the void surface and localized velocity field in the vicinity of the void. On the other hand the results obtained using the equally radial distribution captures the correct deformation features and generates most accurate results. Theoretically, the normal stress σ^{yy} on an infinite plate with a circular void under uniaxial compression loading can be analytically calculated as [3]

$$\sigma^{yy}(x,0) = \sigma_\infty \left(1 + \frac{1}{2}\frac{R_0^2}{x^2} + \frac{3}{2}\frac{R_0^4}{x^4}\right),$$

where σ_∞ is the stress component on the edge of the plate. It is easy to verify from the above equation that for $x >> R_0$, the stress σ^{yy} on the edge of the circular void is about three times greater than the reference stress σ_∞. in Figure 17 we illustrate a comparison between profiles of the normal stress σ^{yy} at $y = 0$ obtained for the considered collocation sets and the theoretical stress. It is clear that for the considered elastodynamic conditions, the results obtained using the

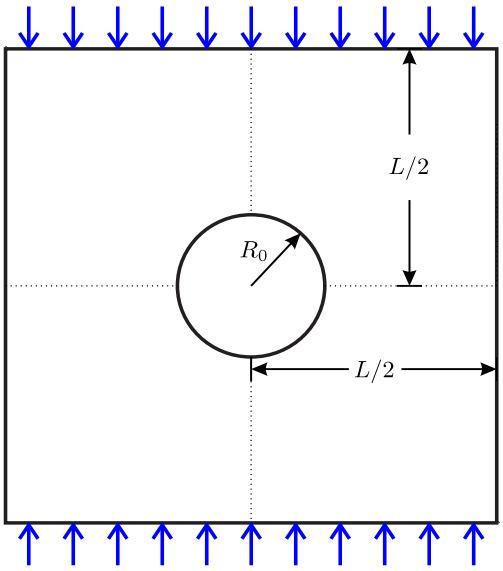

Figure 14: Configuration of the domain for the elastic plate with a void.

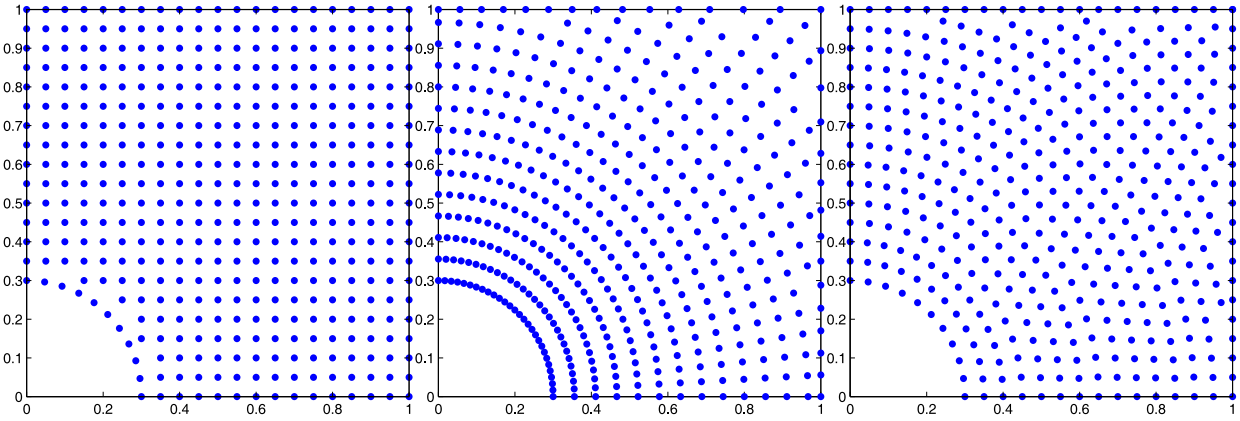

Figure 15: Squared distribution (left) radial distribution (middle) and equally radial distribution (right) of particles for the elastic plate with a void.

equally radial distribution are more accurate than those obtained using the squared and radial distributions. There is a good matching in the profile obtained using the equally radial distribution and the theoretical solution. To quantify the accuracy in these distributions we list in Table 3 the errors for the obtained results in L^1 and L^2 norms. It can be clearly seen that the SPH-RKC method using equally radial distribution accurately solves this problem and it generates less computational errors compared to SPH-RKC method using squared and radial distributions.

Our next concern is to compare the results computed using our SPH-RKC method to those obtained using the conventional finite element method (FEM) for this test example. We consider two sets of simulations with $R_0 = 0.3\ m$ and $R_0 = 0.2\ m$. The meshes used in FEM contain 3025 nodes and 3222 nodes for the case with $R_0 = 0.3\ m$ and $R_0 = 0.2\ m$, respectively. In Figure 18 we present cross-sections of the normal stress σ^{yy} at $y = 0$ and the corresponding errors in L^1 and L^2 norms are summarized in Table 4. A simple examination of the presented results shows that the FEM fails to accurately resolve the case with $R_0 = 0.3\ m$ whereas results obtained using the SPH-RKC method show good agreement with the analytical solution of this elastic plate problem. For a void with small radius $R_0 = 0.2\ m$ both FEM and SPH-RKC method yield comparable

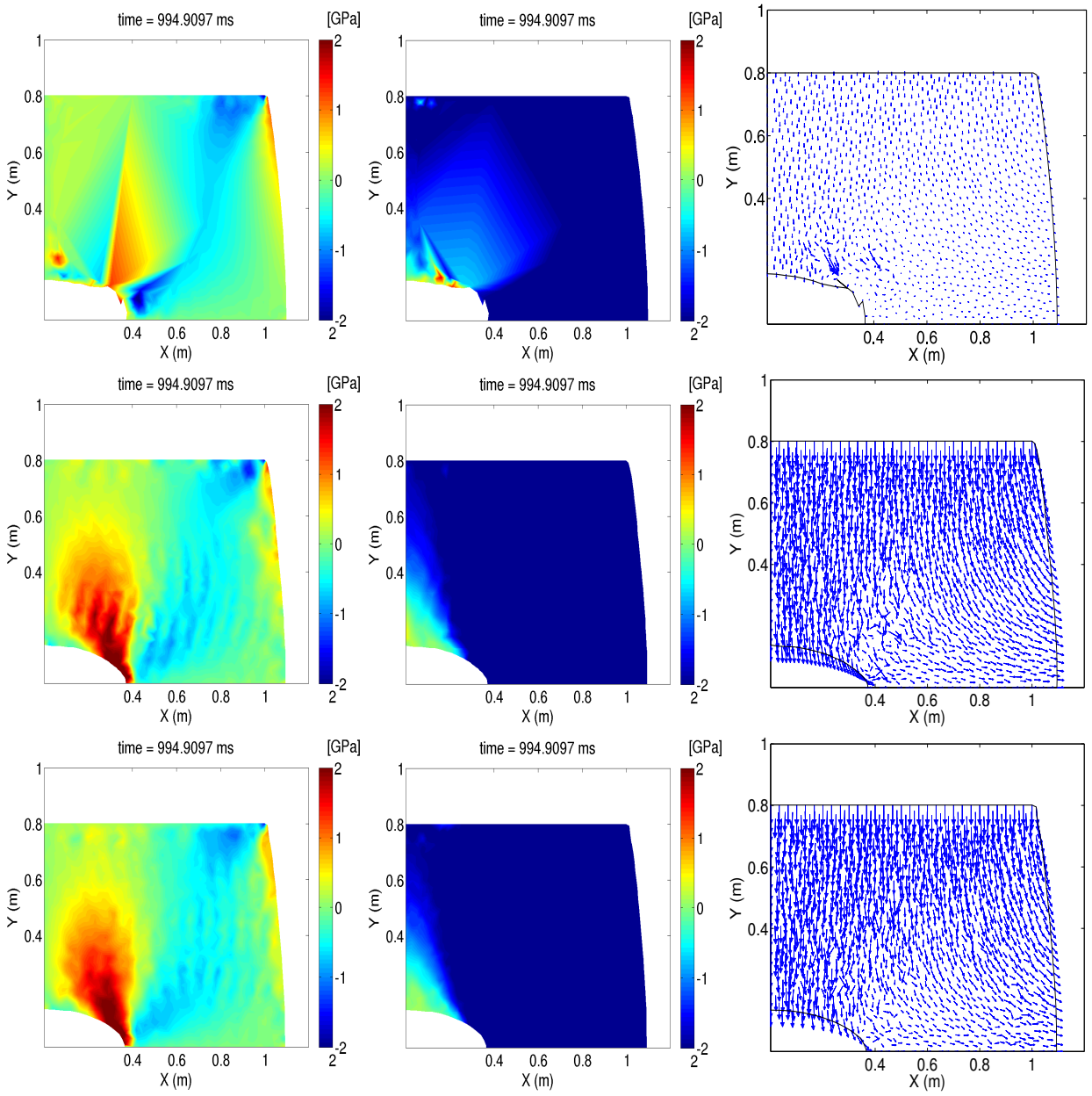

Figure 16: Normal stress σ^{xy} (first column), normal stress σ^{yy} (second column) and velocity field (third column) for the elastic plate with a void using three different collocation sets: Squared distribution (first row), radial distribution (second row) and the equally radial distribution (third row).

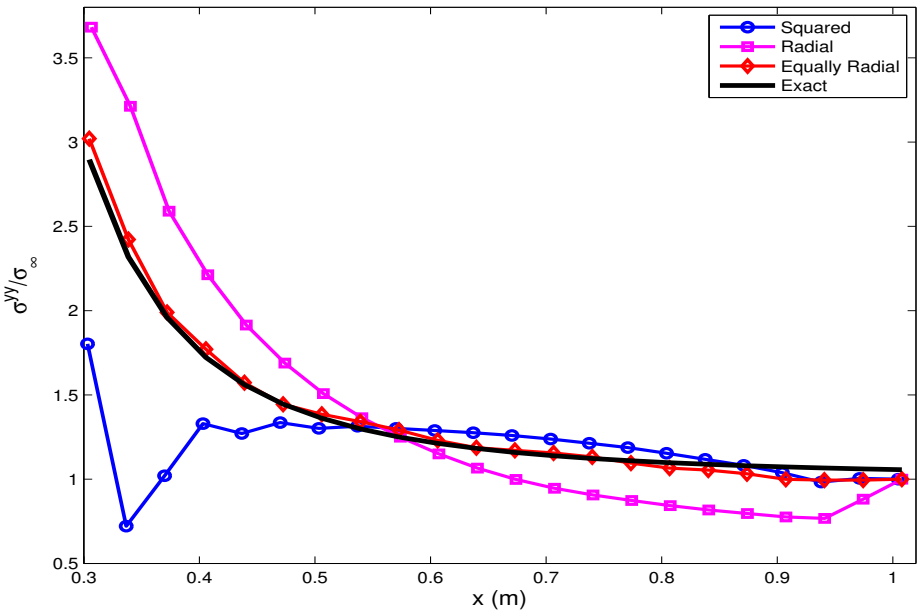

Figure 17: Cross-section at $y = 0$ of the normal stress σ^{yy} for the elastic plate with a void using different particle distributions.

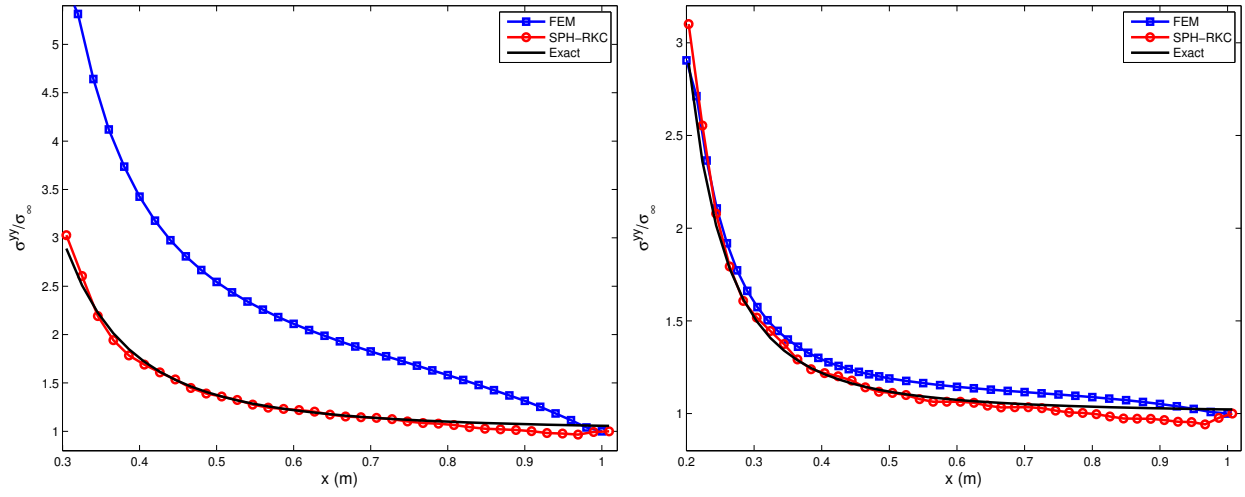

Figure 18: Cross-section at $y = 0$ of the normal stress σ^{yy} using $R_0 = 0.3\ m$ (left) and $R_0 = 0.2\ m$ (right) for the elastic plate with a void.

Table 3: Errors in the cross-section at $y = 0$ of the normal stress σ^{yy} for the elastic plate with a void using different particle distributions.

	Squared distribution	Radial distribution	Equally radial distribution
L^1-error	0.1811	0.2102	0.0307
L^2-error	0.3320	0.2570	0.0375

Table 4: Errors in cross-sections at $y = 0$ of the normal stress σ^{yy} for the elastic plate with a void using FEM and SPH-RKC method. The numbers between brackets refer to the number of nodes in FEM and the number of particles in SHP-RKC method.

	$R_0 = 0.2\ m$		$R_0 = 0.3\ m$	
	FEM (3222)	RKC-SPH (2560)	FEM (3025)	RKC-SPH (2459)
L^1-error	0.0521	0.0304	0.6799	0.0272
L^2-error	0.0537	0.0442	0.8084	0.0357

results but the SPH-RKC results are the most accurate.

Finally we illustrate in Figure 19 the the normal stresses σ^{xy} and σ^{yy}, and the velocity field in the whole domain at three different instants using the equally radial distribution of particles. These plots give a clear view of the overall elastic pattern and the effect of deformation on the structure of normal stresses and velocity fields in the cavity. The new SPH-RKC method performs well for this elastodynamic problem. It is also important to mention two points concerning the number of stages s in the SPH-RKC method. First, the SPH-RKC method requires a large number of stages only when high values of CFL are used in the simulation. Otherwise, two stages are sufficient for low CFL values. This is relevant to the time integration of elsatodynamic problems where wave speed changes within the time from one regime to another. Second, refining of the particle distribution does not mean a decrease in timesteps, since the number of stages in RKC scheme can change. This is a remarkable feature of the SPH-RKC satisfactorily handling procedures using adaptive local particle refinement methods to resolve interfaces for elastodynamics in composite materials.

5 Conclusions

In this paper we have presented a stable explicit Runge-Kutta Chebyshev scheme for the time integration in SPH simulation of elastodynamics. The method uses a class of SPH approximation for discretization in space and it accurately resolves the elastodynamic features regardless whether the deformation is compression or tension dominated. The considered method does not require sever restrictions on the timesteps compared to the conventional explicit time stepping schemes used in conjunction with the SPH method. From a practical viewpoint, the method is straightforward, irrespective of the smoothness of the elastic media and the shape of the domain under consideration, and easy to implement because no mesh is required and only radial distance between neighboring particles is used to approximate the elastodynamic solutions. Validation of the method has been

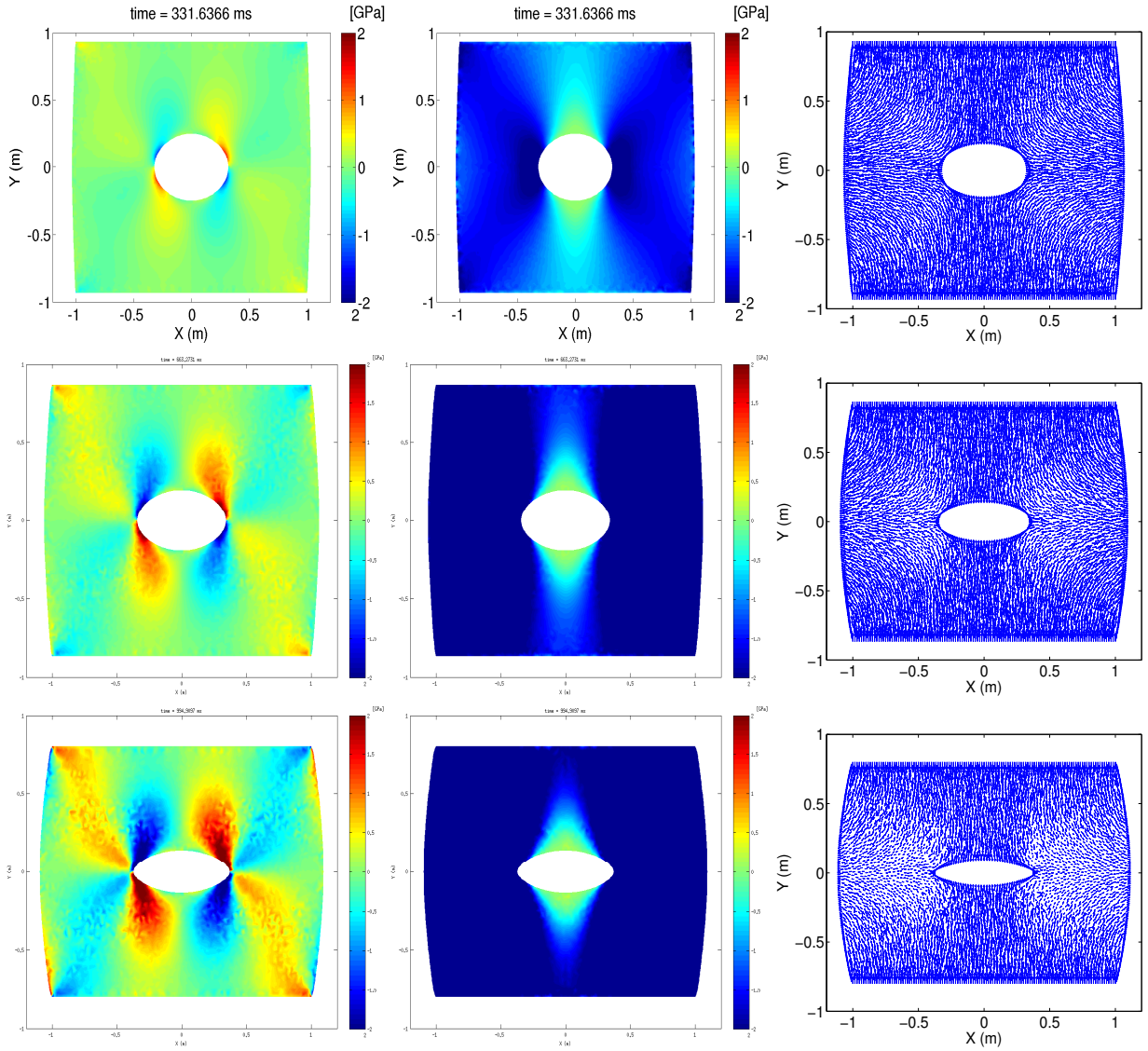

Figure 19: Normal stress σ^{xy} (first column), normal stress σ^{yy} (second column) and velocity fields (third column) using equally radial distribution with 3504 particles at three different times: $t = 331.6336\ ms$ (first row) $t = 663.2731\ ms$ (second row) and $t = 994.9097\ ms$ (third row).

carried out using several test problems on elastodynamics. The numerical results were compared with those obtained using traditional time stepping schemes in SPH simulations. The method was also applied to solve an elastic plate with a void under compression. The method exhibited good shape, high accuracy and stability behavior, even coarse particle distributions and large timesteps are used in computations. Quantitative comparisons have been made with other published works on elastodynamics and a good agreement is found. The presented results demonstrate the capability of the SPH method that can provide insight to complex elastodynamic features. In addition, the computed results for all considered test examples verify the performance and robustness nature of the numerical model.

Future work will concentrate on the extension of the proposed method to elastodynamic in three space dimensions. From a modeling viewpoint, a more realistic model which takes into consideration variations along the depth of elastic domains should be built. The present applications are a relatively idealized two-dimensional model where only the depth-averaged variation is modeled. A more realistic model with the use of Runge-Kutta Chebyshev SPH method is currently being investigated. Future work will also concentrate on extending the proposed techniques for nonlinear problems in elastodynamics.

References

[1] C. Altomare, A.J.C Crespo, B.D. Rogers, J.M. Dominguez, X. Gironella, and M. Gomez-Gesteira. Numerical modelling of armour block sea breakwater with smoothed particle hydrodynamics. *Computers and Structures*, 130:34–45, 2014.

[2] D.N. Arnold and J.J. Lee. Mixed methods for elastodynamics with weak symmetry. *SIAM J. Numer. Anal.*, 50(6):2743–2769, 2014.

[3] M.F. Ashby and D.R.H. Jones. *Engineering Materials 2.* Elsevier, 2013.

[4] S.N. Atluri and T. Zhu. A new meshless local Petrov-Galerkin (MLPG) approach in computational mechanics. *Computational Mechanics*, 22:117–127, 1998.

[5] H. H. Bui, R. Fukagawa, K. Sako, and S. Ohno. Lagrangian meshfree particles method (SPH) for large deformation and failure flows of geomaterial using elastic-plastic soil constitutive model. *International journal for numerical and analytical methods in geomechanics*, 32:1537–1570, 2008.

[6] H. H. Bui, R. Fukagawa, K. Sako, and J. C. Wells. Slope stability analysis and discontinuous slope failure simulation by elasto-plastic smoothed particle hydrodynamics (SPH). *Geotechnique*, 61(7):565–574, 2011.

[7] P.J. Van der Houwen. Explicit Runge-Kutta formulas with increased stability boundaries. *Numer. Math.*, 20:149–164, 1972.

[8] P.J. Van der Houwen and B.P. Sommeijer. On the internal stability of explicit, m-stage Runge-Kutta methods for large m-values. *Z. Angew. Math. Mech.*, 60:479–485, 1980.

[9] M. Doring, G. Oger, B. Alessandrini, and P. Ferrant. SPH simulations of floating bodies in waves. *In: Proc. international workshop on water waves and floating bodies (IWWWFB), Cortona, Italy*, 2004.

[10] C. T. Dyka and R. P. Ingel. An approach for tension instability in smoothed particle hydrodynamics (SPH). *Computers and Structures*, 57:573–580, 1995.

[11] C. T. Dyka and P. W. Randles. Stress points for tension instability in SPH. *International Journal of Numerical Methods in Engineering*, 39:2725–2741, 1996.

[12] R.A. Gingold and J.J. Monaghan. Smoothed particles hydrodynamics: theory and application to non-spherical stars. *Monthly Notices of the Royal Astronomical Society*, 181:375–389, 1977.

[13] M. Gomez-Gesteira, B.D. Rogers, A.J.C. Crespo, R.A. Dalrymple, and M. Narayanaswamy. SPHysics development of a free-surface fluid solverpart 1: Theory and formulations. *Computers and Geosciences*, 48:289–299, 2012.

[14] J. P. Gray, J. J. Monaghan, and R. P. Swift. SPH elastic dynamics. *Computational Methods in Applied Mechanics and Engineering*, 190:6641–6662, 2001.

[15] L. Hernquist and N. Katz. TreeSPH- a unification of SPH with the hierarchical tree method. *Astrophysical Journal Supplement Series*, 70:419–446, 1989.

[16] W.G. Hoover and C.G. Hoover. Spam-based recipes for continuum simulations. *Computing in Science and Engineering*, 3(2):78–85, 2001.

[17] C.B. Kandilas. Transient elastodynamic analysis of nonhomogeneous anisotropic plane bodies. *Acta Mechanica*, 223:861–878, 2012.

[18] L.D Landau and E.M. Lifshitz. *Theory of Elasticity.* Volume 7. Pergamon Press, 2nd ed. edition, 1970.

[19] L. D. Libersky, A. G. Petschek, T. C. Carney, J. R. Hipp, and F. A. Allahdadi. High strain lagrangian hydrodynamics: a three dimensional SPH code for dynamic material response. *Journal of Computational Physics*, 109:67–75, 1993.

[20] G.R. Liu and M.B. Liu. *Smoothed particles hydrodynamics: A Meshfree Particle Method.* World Scientific Publishing, Singapore, 2004.

[21] M.B. Liu and G.R. Liu. Smoothed particle hydrodynamics (SPH): an overview and recent developments. archives of computational methods in engineering. *Monthly Notices of the Royal Astronomical Society*, 17(1):25–76, 2010.

[22] L.B. Lucy. A numerical approach to the testing of the fission hypothesis. *Astronomical Journal*, 82(12):1013–1024, 1977.

[23] D. Mirzaei and K. Hasanpour. Direct meshless local Petrov-Galerkin method for elastodynamic analysis. *Acta Mechanica*, 276:1–14, 2015.

[24] J. J. Monaghan. Simulating free surface flows with SPH. *Journal of Computational Physics*, 110:399–406, 1994.

[25] J. J. Monaghan. SPH without a tensile instability. *Journal of Computational Physics*, 159:290–311, 2000.

[26] J. J. Monaghan and J. C. Lattanzio. A refined particle method for astrophysical problems. *Astro. Astrophys*, 149:135–143, 1985.

[27] J.J. Monaghan. On the problem of penetration in particle methods. *Journal of Computational Physics*, 82:1–15, 1989.

[28] J.J. Monaghan. Smoothed particle hydrodynamics. *Annual Review of Astronomical and Astrophysics*, 30:543–574, 1992.

[29] J. P. Morris, P. J. Fox, and Y. Zhu. Modeling low reynolds number incompressible flows using SPH. *Journal of Computational Physics*, 136:214–226, 1997.

[30] P. W. Randles and L. D. Libersky. Smoothed particle hydrodynamics: some recent improvements and applications. *Computational Methods in Applied Mechanics and Engineering*, 139(1-4):375–408, 1996.

[31] P. W. Randles and L. D. Libersky. Normalized SPH with stress points. *International Journal of Numerical Methods in Engineering*, 48:1445–1462, 2000.

[32] M. Robinson. Turbulence and viscous mixing using smoothed particle hydrodynamics. *Monash University*, 2009.

[33] E.J. Sellountos, A. Sequeira, and D. Polyzos. A new LBIE method for solving elastodynamic problems. *Engineering Analysis with Boundary Elements*, 35(2):185–190, 2011.

[34] J.R. Shao, H.Q. Li, G.R. Liu, and M.B. Liu. An improved sph method for modeling liquid sloshing dynamics. *Computers & Structures*, 100-101:18–26, 2012.

[35] S. Srivastava. Mixed discontinuous Galerkin methods: Application to nonlinear elastodynamics. *Ph.D. thesis in State University OF New York at Buffalo*, 2008.

[36] H. Takeda, S. M. Miyama, and M. Sekiya. Numerical simulation of viscous flow by smoothed particle hydrodynamics. *Progress of Theoretical Physics*, 92(5):939, 1994.

[37] J.G. Verwer, W.H. Hundsdorfer, and B.P. Sommeijer. Convergence properties of the Runge-Kutta-Chebychev method. *Numer. Math.*, 57:157–178, 1990.

[38] R. Vignjevic, J.R. Reveles, and J. Campbell. SPH in a total lagrangian formalism. *Comput. Model. Eng. Sci.*, 14(3):181198, 2006.

[39] D. Violeau and A. Leroy. Optimal time step for incompressible SPH. *Journal of Computational Physics*, 288:119–130, 2015.

[40] A. Zhang, F. Ming, and X. Cao. Total lagrangian particle method for the large-deformation analyses of solids and curved shells. *Acta Mechanica*, 225:253–275, 2014.

[41] A. Zhang, P. Sun, and F. Ming. An SPH modeling of bubble rising and coalescing in three dimensions. *Computer Methods in Applied Mechanics and Engineering*, 294:189–209, 2015.